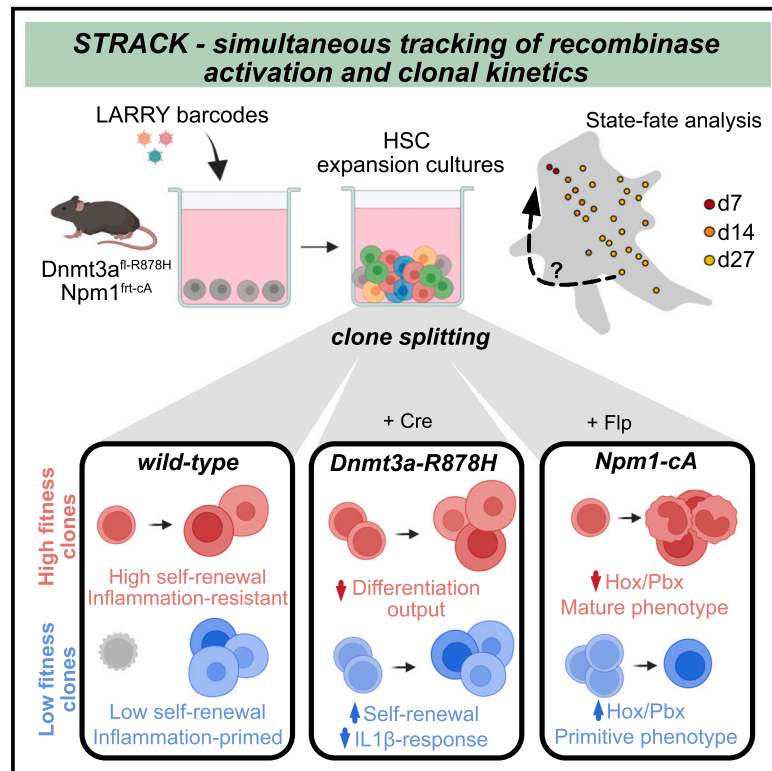


# Cell Stem Cell

## Pre-existing stem cell heterogeneity dictates clonal responses to the acquisition of leukemic driver mutations

### Graphical abstract



### Authors

Indranil Singh,  
Daniel Fernandez-Perez,  
Pedro Sanchez Sanchez,  
Alejo E. Rodriguez-Fraticelli

### Correspondence

alejo.rodriquez-fraticelli@  
irbbarcelona.org

### In brief

Singh, Fernandez-Perez, et al. use hematopoietic stem cell barcoding to study clones with and without activation of cancer driver mutations, identifying that pre-existing stem cell states can dictate resulting (pre-)cancerous phenotypes and showing that inflammation-sensitive stem cells can be a powerful source of malignant evolution.

### Highlights

- Single-cell tracing of cancer initiation at the clonal level
- *Ex vivo* expansion cultures sustain intrinsic and heritable HSC heterogeneity
- *Dnmt3a* mutation prevents inflammatory exhaustion of differentiation-primed stem cells
- *Npm1c* reprograms differentiation-primed stem cells into more primitive malignant states



Article

# Pre-existing stem cell heterogeneity dictates clonal responses to the acquisition of leukemic driver mutations

Indranil Singh,<sup>1,2,4</sup> Daniel Fernandez-Perez,<sup>1,4</sup> Pedro Sanchez Sanchez,<sup>1</sup> and Alejo E. Rodriguez-Fraticelli<sup>1,3,5,\*</sup>

<sup>1</sup>Institute for Research in Biomedicine (IRB Barcelona), The Barcelona Institute of Science and Technology, Barcelona, Catalonia, Spain

<sup>2</sup>Facultat de Biologia, Universitat de Barcelona, Barcelona, Catalonia, Spain

<sup>3</sup>ICREA, Catalan Institution for Research and Advanced Studies Barcelona, Barcelona, Catalonia, Spain

<sup>4</sup>These authors contributed equally

<sup>5</sup>Lead contact

\*Correspondence: [alejo.rodriquez-fraticelli@irbbarcelona.org](mailto:alejo.rodriquez-fraticelli@irbbarcelona.org)

<https://doi.org/10.1016/j.stem.2025.01.012>

## SUMMARY

Cancer cells display wide phenotypic variation even across patients with the same mutations. Differences in the cell of origin provide a potential explanation, but traditional assays lack the resolution to distinguish clonally heterogeneous subsets of stem and progenitor cells. To address this challenge, we developed simultaneous tracking of recombinase activation and clonal kinetics (STRACK), a method to trace clonal dynamics and gene expression before and after the acquisition of cancer mutations. Using mouse models, we studied two leukemic mutations, *Dnmt3a*-R878H and *Npm1c*, and found that their effect was highly variable across different stem cell states. Specifically, a subset of differentiation-primed stem cells, which normally becomes outcompeted with time, expands with both mutations. Intriguingly, *Npm1c* mutations reversed the intrinsic bias of the clone of origin, with differentiation-primed stem cells giving rise to more primitive malignant states. Thus, we highlight the relevance of single-cell lineage tracing to unravel early events in cancer evolution and posit that different cellular histories carry distinct cancer phenotypic potential.

## INTRODUCTION

Cancer cells display striking phenotypic variation, within and across patients, yet the origins of this variation are still unclear.<sup>1</sup> Since cancer is a clonal disorder, researchers have long hypothesized that phenotypic heterogeneity could be a consequence of the cell type that acquires the driver mutations.<sup>2,3</sup> The “cell-of-origin” model revolutionized the cancer field, leading to transformational discoveries across various tumor types.<sup>4–6</sup> The cell-of-origin hypothesis has been extensively characterized in cancer types with few driver mutations, such as myeloid malignancies. Depending on whether mutations are introduced in the hematopoietic stem cells (HSCs), at the top of the hematopoietic hierarchy, or in the more mature myeloid progenitors (MPs), researchers have consistently shown differences in the resulting phenotypes.<sup>7–16</sup> However, traditional cell-of-origin studies induce mutations at the population level using reporter genes or surface markers, which are insufficient to discretize the complex heterogeneity in the system.<sup>17,18</sup> Furthermore, we and others have shown that even the HSCs, at the top of the hierarchy, are biased at the level of both state and function, with a multiplicity of fate-imprinted clonal hierarchies co-existing in the bone marrow (BM).<sup>19–29</sup> Importantly, due to the lack of high-resolution cell-of-origin techniques, the functional significance of stem cell heterogeneity in tumor initiation remains poorly understood,<sup>30</sup> leaving researchers to rely on inference.<sup>31</sup>

Here, we present a system called simultaneous tracking of recombinase activation and clonal kinetics (STRACK), which precisely addresses existing methodological and knowledge gaps, unbiasedly linking pre-existing stem cell states (and intrinsic fates) with their potential cancer states and fates. STRACK takes advantage of defined primary stem cell culture systems to explicitly minimize the confounding effect of extrinsic variables and solely focus on intrinsic determinants. To this end, STRACK combines long-term *ex vivo* PVA-based expansion cultures, which can sustain and expand HSCs and myeloid progeny for weeks,<sup>32,33</sup> mouse models carrying different *Cre/Flp*-inducible leukemia mutations,<sup>34</sup> a second-generation palette of Lineage and RNA Recovery (LARRY) barcode libraries to track clones, and a sister-cell-clone-splitting strategy.<sup>24,29</sup> This unique combination allowed us to sample the system longitudinally and obtain a dense clonal and transcriptional landscape for the same set of clones, with and without mutations.

## RESULTS

### State-fate analysis in long-term PVA-based HSC expansion cultures

In order to characterize HSC clonal behaviors in PVA-based *ex vivo* expansion cultures, we profiled thousands of HSC clones through a 27-day protocol using single-cell lineage tracing and RNA profiling. For this, we genetically labeled ~10,000 long-term



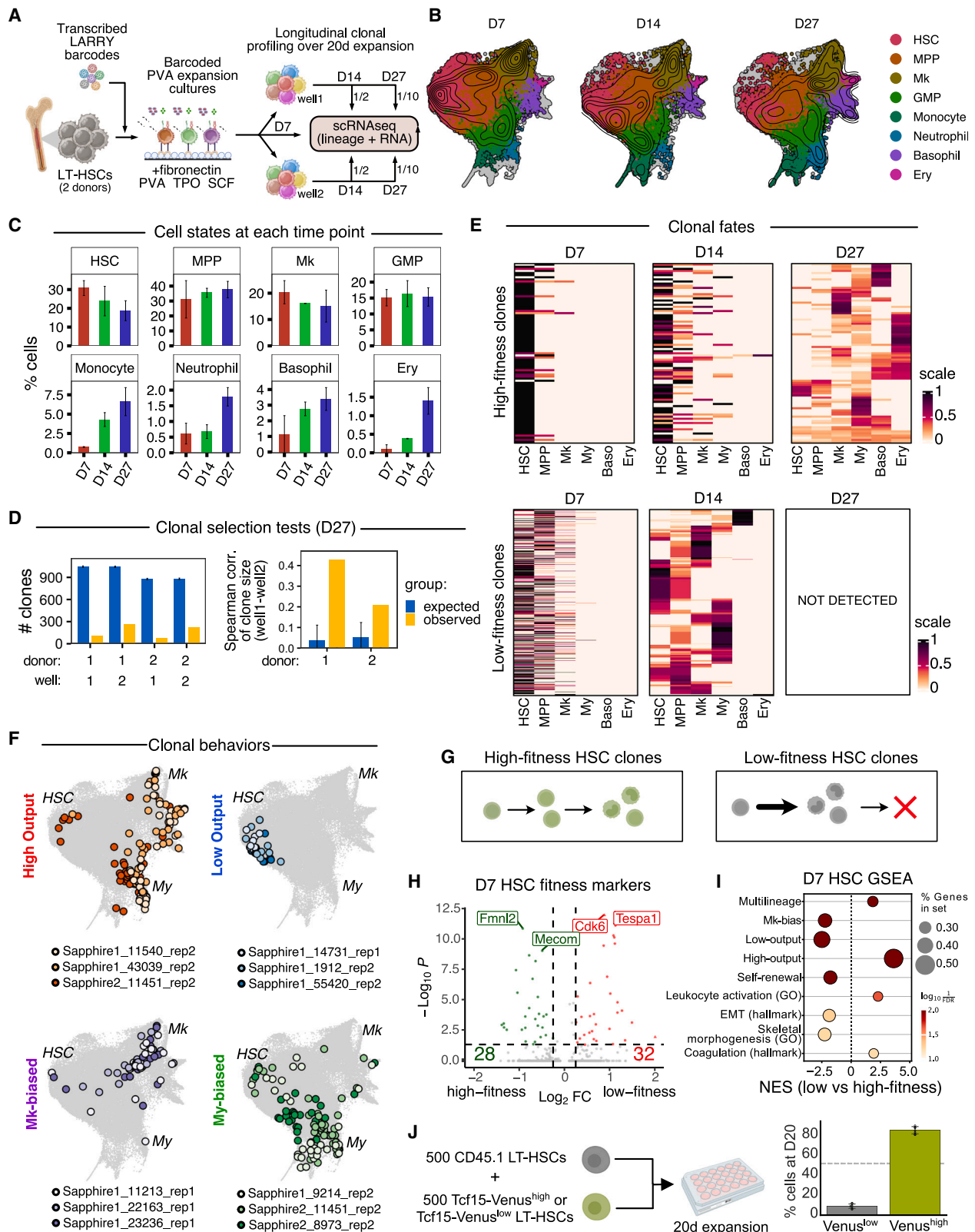


**Figure 1. State-fate analysis in ex vivo HSC expansion cultures**

(A) Experimental design. HSCs transduced with the LARRY barcode library were cultured for up to 27 days. Cells were sampled at different time points by scRNA-seq to profile lineage (barcode) and state.

(legend continued on next page)

HSCs (lineage— Sca-1+ cKit+ CD48— CD150+ CD201+ or “E-SLAM”) with second-generation LARRY barcoding libraries expressing the T-Sapphire fluorescent protein (Figure S1A). Labeled HSCs were expanded across multiple wells for 27 days, sorted, and randomly sampled for scRNA-seq as depicted in the schematic at days 7, 14, and 27 (Figure 1A; Table S1 ~see STAR Methods).<sup>24</sup>

Most of the cells profiled on day 7 expressed markers of HSCs (*Procr*, *Hlf*, and *Mecom*) or multipotent progenitors (MPPs, *Cd48*) (Figure S1B). Starting on day 14, but mostly at day 27, we also found a continuum of differentiating cell states that we annotated using marker genes to six major cluster groupings: granulocyte monocyte progenitors (GMPs), megakaryocyte progenitors (Mk), erythrocyte progenitors (Ery), basophil progenitors (Ba), monocyte progenitors (Mono), and neutrophil progenitors (Neu) (Figures 1B, 1C, and S1B—markers detailed in Table S2). Even at day 27, we could still annotate thousands of cells as HSCs, confirming their expansion within these cultures (Figures 1C and S1C). This result suggested both differentiation and self-renewal from the initial pool of stem cells as previously reported.<sup>32,33</sup>

Next, we leveraged LARRY barcoding to assess the clonal dynamics and cell fate choices of expanded HSCs over time. We found that expansion cultures gradually lose their clonality, despite initiating from highly pure EPCR+ HSCs, in line with recent reports (Figure 1D).<sup>35</sup> Sister-cell splitting across independent wells confirmed the preferential expansion of specific clones, which correlated across wells higher than expected based on a null distribution obtained from a sampling simulation (Figures 1D and S1D).

To describe the mechanisms leading to clonal selection, we visualized all clones detected in both D7 and D14 time points using “clone x annotation” fate heatmaps, which are colored based on the fate bias in each individual clone (Figure 1E). We observed a striking heterogeneity in fate biases across clones even at D27 (Figures 1F and S1C). We next quantified HSC clonal fate properties based on our previous methodology.<sup>36</sup> Briefly, output activity (the ratio of differentiation versus self-renewal) was calculated as the frequency of clone *i* non-HSC clusters divided by the frequency of clone *i* in the HSC cluster. Specific fate biases (megakaryocyte and myeloid)

were quantified as the frequency of clone *i* in the cluster *k* divided by the frequency of the clone *i* across non-*k* clusters. Fate-biased HSCs showed differences in gene expression programs, which resembled those previously identified in transplant or developmentally traced native hematopoiesis and showed hallmarks of heritability (Figures S1E–S1H).<sup>19,36</sup> Together, these results indicate the preservation of clonal HSC fate and state heterogeneity in long-term *ex vivo* HSC expansion cultures.

We next compared the HSC clones that persist and expand until D27 (termed “high-fitness clones”) with the clones that are detected early (at day 7 and 14) but do not expand enough to be detected at the last time points (termed “low-fitness clones”). Analysis of their fate properties indicated that out-competed, low-fitness clones displayed more rapid and abundant contribution to mature progeny, suggesting intrinsic priming for activation and differentiation (Figures 1E, S1I, and S1J). To assess the early transcriptional differences associated with these differences in fitness, we used longitudinal retrospective state-fate analysis, comparing the HSC cell states at day 7 based on their fitness differences at day 27 (Figures 1G and 1H; Table S3). High-fitness HSCs exhibited enriched expression of markers associated with self-renewal (*Procr*) and HSC identity (*Mecom*, *Ly6a*, and *Hlf*), as well as non-conventional retinoic signaling (*Rarb*), extracellular matrix (*Sdc4* and *Mmp16*), synapses (*Dlg2* and *Ncam2*) and actin cytoskeleton regulation (*Fmn12*, *Gimp*, and *Palld*) (Figure 1H). High-fitness HSC clones also expressed higher levels of low-output and Mk-biased HSC signatures, as well as Skeletal morphogenesis signatures (*Tcf15* and *Myof*) (Figure 1I and Table S4). To validate the high fitness of *Tcf15*<sup>high</sup> cells during *ex vivo* HSC cultures, we used the *Tcf15*-Venus mouse model, which enriches for highly transplantable self-renewing HSCs.<sup>36</sup> We sorted 500 CD45.1 wild-type (WT) E-SLAM HSCs and co-cultured them with either *Tcf15*<sup>high</sup> or *Tcf15*<sup>low</sup> E-SLAM HSCs (marked by their CD45.2 background). *Tcf15*<sup>high</sup> HSCs consistently expanded more than the bulk HSCs, whereas *Tcf15*<sup>low</sup> cells were relatively outcompeted after 20 days in expansion cultures (Figure 1J). Taken together, these analyses indicate that *ex vivo* expansion cultures display a broad range of stable and dynamic fate behaviors, including intrinsic and deterministic differences in

(B) UMAP of wild-type (WT) cell states in *ex vivo* expansion cultures from days 7, 14, and 27 time points. Cells are colored based on their cluster annotations. Density overlay indicates the density of cells across the UMAP.

(C) Cluster distribution of WT *ex vivo* expansion cultures at different time points. The mean and SD of two independent experiments are represented.

(D) Evidence for clonal selection. Left, observed versus expected number of clones per well at day 27 based on a stochastic sampling model. Right, Spearman correlation of sister-cell clone sizes across split independent wells (observed, yellow; blue, expected;  $n = 1,000$  simulations, mean  $\pm$  SD).

(E) State-bias heatmaps showing clones (rows) and clusters/states (columns), colored by the intra-clonal fraction in each cluster/state (scale). Clones shown are all those detected in both days 7 and 14. Clones are separated into two heatmaps (top—bottom), depending on whether the clone is detected (in at least 2 cells) at day 27.

(F) UMAP showing example WT clonal behaviors at day 27 from different experiments/replicates. High or low output refers to the ratio of differentiation (frequency of mature progeny) over self-renewal (frequency of HSCs). Three different clones for each clonal behavior are represented, colored by clone of origin.

(G) Scheme of the interpretation of results based on clonal groupings. In the final sampling point, low-fitness clones cannot be detected anymore (they get exhausted), while high-fitness clones continue to survive and expand (possibly driven by higher self-renewal).

(H) Volcano plot for day 7 HSCs comparing low-versus-high fitness clonal groups. Selected genes are highlighted. Markers associated with each group are shown in green (high-fitness) or red (low-fitness). Bottom red and green numbers represent the number of downregulated and upregulated genes, respectively.

(I) Gene set enrichment analysis (GSEA) of differential gene expression results in (H). Scale is  $\log_{10}$  FDR<sup>-1</sup>.

(J) Competitive 1:1 *ex vivo* HSC expansion of *Tcf15*-Venus<sup>high</sup> or *Tcf15*-Venus<sup>low</sup> HSCs co-cultured with CD45.1 HSCs. Right, quantification of CD45.2+ fraction at day 20 (mean  $\pm$  SD,  $n = 5$ ,  $p < 0.001$ ).

See also Tables S1, S2, S3, and S4.

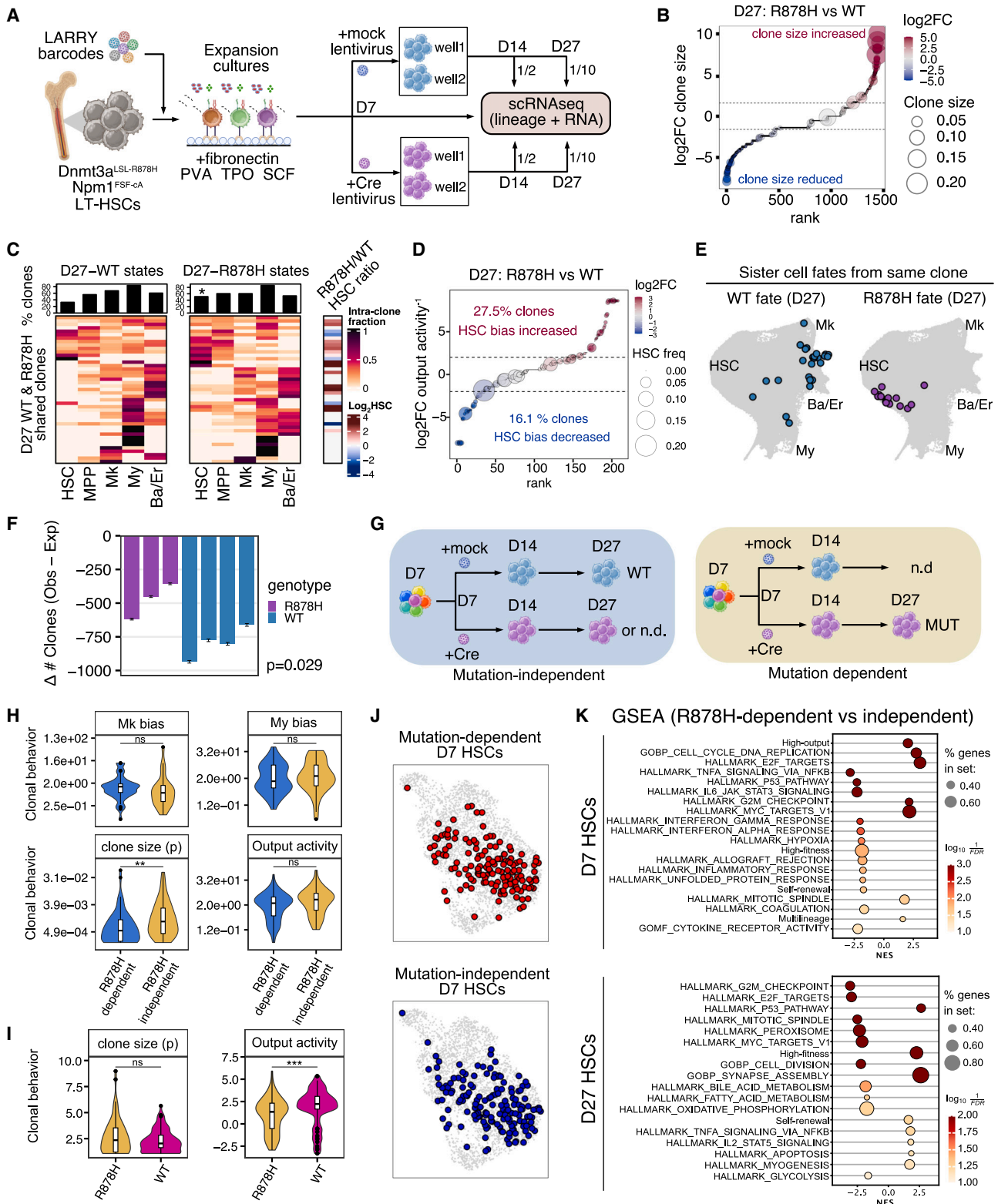


**Figure 2. Sister-cell state-fate landscape of Dnmt3a-R878H mutagenesis**

(A) Experimental design for sister-cell state-fate analysis in R878H mutagenesis.

(B) Waterfall plot showing log<sub>2</sub> fold-change in clone size (fraction of cells) for the same set of clones with and without the R878H mutation. Red color indicates increased clone size upon mutation while blue color indicates decreased clone size upon mutation. Bubble size indicates size of the clone in the condition where it was larger.

(legend continued on next page)

fitness, which allows us to study how different stem cell clones respond upon acquisition of cancer driver mutations, which should increase this fitness.

### Sister-cell analysis and state-fate landscapes for Dnmt3a-R878H mutagenesis

To investigate how different cancer driver mutations influence stem cell fates, we used a mouse model carrying two different conditional knockin mutations that can be activated using different recombinases: a Cre-dependent Dnmt3a-R878H mutation (R878H) and a Flp-dependent Npm1-cA mutation (Npm1c). We started by studying the effects of R878H, the mouse homolog of Dnmt3a-R882H, which is one of the most frequent driver mutations in acute myeloid leukemia (AML).<sup>34,37</sup> To activate the R878H mutation, we developed a second set of lentiviral libraries constitutively expressing Cre-recombinase and a fluorescent reporter or the mock fluorescent reporter alone as a control (Cre-P2A-mScarlet and mScarlet). We isolated HSCs from male and female mice, transduced them with differently indexed T-Sapphire LARRY libraries, and then, on day 7, we profiled a part of the cells and split the remainder into a Cre or a mock labeling reaction, and then these were further split into separate wells that continued expansion independently (Figure 2A). The system allowed state-fate analysis for both WT and mutant clones arising from sister HSCs, which we termed STRACK.

We observed increased expansion of Dnmt3a R878H mutant cells (from here on R878H cells) in competitive cultures (Figure S2A) but did not identify major differences in their states (at the population level) compared with WT mock controls from the same mouse line (Figure S2B). After performing clonal analysis, we observed that HSC clones expanding significantly more with R878H also tended to have the largest clone sizes (Figure 2B). We then compared the clones that could be detected in both day 7 as well as day 27 in both WT and R878H cells by plotting their behaviors using state-bias heatmaps (Figure 2C). Sister WT/R878H clones displayed remarkably similar behaviors, even with a mutation and 20 days after splitting. However, this analysis showed a clear difference: most clones gained relatively more HSCs with R878H mutation in comparison to WT (Figure 2D), which resulted in reduced clonal output activity (Fig-

ure S2C). In some rare but notable cases, high-output multilineage clones even completely lost their output in the presence of the R878H mutation (Figure 2E), indicating that differentiation-biased stem cells can be efficiently reprogrammed by the Dnmt3a mutation to increase their self-renewal at the expense of differentiation.

Considering these effects, we wondered whether the mutation could be altering the fitness capacity of intrinsically low-fitness clones, which differentiate early and get outcompeted during long-term culture. Comparing the clonality of R878H cultures with sampling simulations confirmed that R878H cultures maintained a relatively more polyclonal pool ( $p = 0.029$ ), suggesting that clones that are normally outcompeted in the WT setting can persist upon activation of the R878H mutation (Figure 2F). We next compared the clones detected at day 14 and day 27 only in R878H cells (mutation-dependent) with those detected only in WT or in both WT and R878H conditions at day 14 and day 27 (mutation-independent) (Figure 2G). We plotted state-bias heatmaps for day 27 states for each clone, split into groups based on their detection in WT and/or R878H cultures (Figure S2D). Surprisingly, mutation-dependent R878H clones at day 27 behaved similarly compared with mutation-independent R878H clones (Figure 2H), with increased HSC bias compared with WT-only clones (Figure 2I). We next used retrospective state-fate analysis and compared the transcriptomes of day 27 HSCs based on their R878H mutation dependency at day 27 (Figure 2J). Gene set enrichment analysis (GSEA) of R878H-dependent versus independent clones at day 7 indicated reduced expression of self-renewal and fitness signatures, supporting the origin of mutation-dependent clones in low-fitness HSCs (Figure 2K, top). In line with the fate bias analyses, post-mutation R878H-dependent HSCs displayed positive enrichment of high-fitness and self-renewal signatures, indicating the potent stemness reprogramming capacity of these driver mutations (Figure 2K, bottom). We further confirmed this by quantifying the single-cell low-fitness scores of R878H-dependent and independent HSCs at day 7 and 27 (Figure S2E). In addition to changes in HSC output, differential expression analysis and GSEA revealed that R878H HSCs (and MPPs) displayed reduced expression of early response genes, suggesting dampened

(C) State-bias heatmap of clones ( $n = 43$ ) observed in both WT and R878H cultures at day 27.  $\log_2$  fold-change in HSC bias is shown on the right. Each row corresponds to a single barcode (clone), and these are aligned to show the same clone in both conditions, colored by intra-clone fraction (scale). Clones (rows) are ordered by hierarchical clustering (using scaled data from both conditions for every clone). Bars on top of the heatmap correspond, for each individual column, to the percentage of clones in which a barcode has been detected for that specific cell type. Notice the increased percentage of HSCs in R878H cultures (marked by an asterisk).

(D) Waterfall plot showing  $\log_2$  fold-change in HSC versus mature bias (output activity<sup>-1</sup>) for the same set of clones comparing R878H versus WT. Scale is red (higher self-renewal in R878H condition) to blue (higher self-renewal in WT). Bubble size indicates the HSC frequency in the condition where it was higher.

(E) Example UMAP of sister wild-type and mutant fates for the same clone (all cells were derived from a single HSC at the time of barcoding).

(F) Difference between observed and expected number of clones at day 27, based on the stochastic sampling model. Mean  $\pm$  SD,  $n = 1,000$  simulations,  $p < 0.029$ .

(G) Schematic for grouping clones as mutation-dependent or mutation-independent.

(H) Box plots comparing clone size proportion ( $p$ ), output activity, and fate bias (megakaryocytic or myeloid) in R878H-dependent ( $n = 82$  clones) and R878H-independent ( $n = 47$  clones) mutant clones at day 27.  $**p < 0.01$ , ns, not significant.

(I) Box plots comparing clone size and output activity in R878H-dependent (R878H-only,  $n = 82$ ) and WT-only ( $n = 95$ ) clones at day 27.  $***p < 0.005$ , ns: not significant.

(J) UMAP of HSCs at day 7. Highly variable genes, principal components, and UMAP coordinates have been recomputed specifically for HSCs. D7 clones detected at day 27 are highlighted (R878H-dependent, top; R878H-independent, bottom).

(K) GSEA of differential gene expression results comparing R878H-dependent versus independent clones (day 7, before mutation, top; day 27, after mutation, bottom). Scale is  $\log_{10}$  FDR<sup>-1</sup>.

See also Tables S1, S2, S3, and S4.

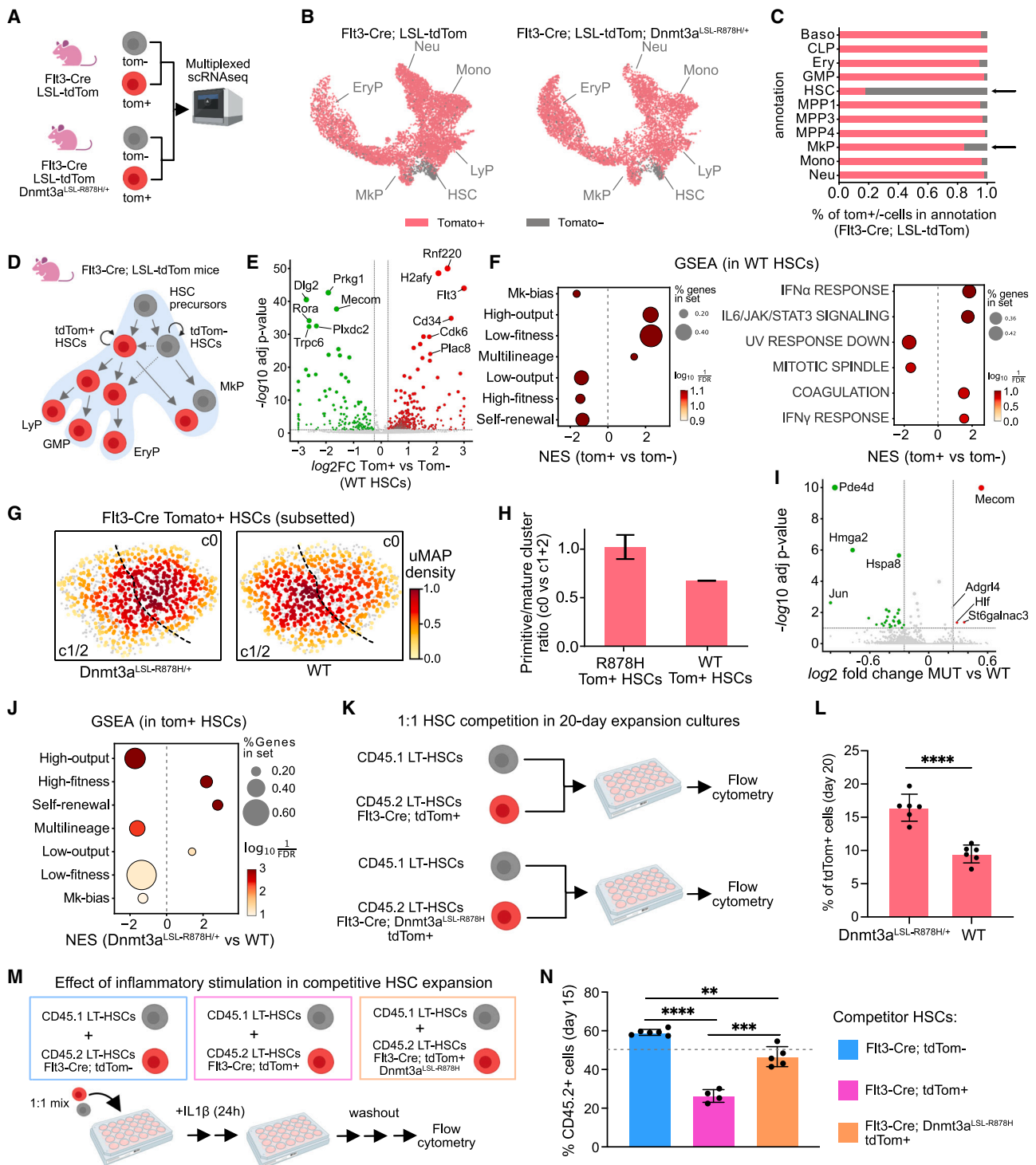


**Figure 3. Dnmt3a-R878H rewires stem cell fitness in the Flt3-Cre HSC model**

(A) Experimental design for analysis of Flt3-Cre HSC models with sample-hashed scRNA-seq.  
 (B) UMAP showing Flt3-Cre wt and Flt3-Cre R878H hematopoietic landscapes, with cells colored by tdTom expression. Annotated cluster groups are indicated.  
 (C) Barplot of an exemplary sample showing cluster distribution of tdTom<sup>+</sup> and tdTom<sup>-</sup> cells.  
 (D) Scheme showing interpretation of Flt3-Cre model results.  
 (E) Volcano plot showing differential expression analysis of Flt3-Cre tdTom<sup>+</sup> versus tdTom<sup>-</sup> HSCs.  
 (F) GSEA showing hallmarks and HSC signatures for Flt3-Cre tdTom<sup>+</sup> versus tdTom<sup>-</sup> HSCs. Scale is log<sub>10</sub> FDR<sup>-1</sup>.

(legend continued on next page)

inflammatory activation as an additional mechanism for their competitive expansion, in line with recent reports in clonal hematopoiesis (Figures S2F and S2G).<sup>38–40</sup> Together, these results highlight the differential effect of this cancer driver mutation across different stem cell clones. While the effects of the R878H mutation are too mild to affect the intrinsically high-fitness clones, it can potentially reprogram the fates and states of low-fitness HSCs, allowing them to survive and expand in *ex vivo* long-term cultures.

### The Flt3-Cre model recapitulates Dnmt3a-R878H mutagenesis in low-fitness HSCs

Next, we sought to validate the fitness reprogramming effects of the Dnmt3a R878H mutation using a complementary approach to identify these cells. We and others have previously identified *Flt3* as part of the gene signature of high-output, multilineage HSCs.<sup>36,41</sup> Although no HSCs express the Flt3 receptor on their surface, we hypothesized that the cells could still be identified using a transcriptional reporter, the *Flt3-Cre* allele, in which *Flt3*-expressing cells can acquire a label through concomitant expression of Cre recombinase.<sup>42</sup> In previous studies, using mTmG or LSL-EYFP reporters, researchers reported that Flt3-Cre only labels developmentally restricted HSCs (which disappear after birth), and it does not label any adult HSCs.<sup>43,44</sup> However, we speculated that, in combination with a more sensitive reporter, the LSL-TdTomato allele (tdTom), Flt3-Cre could still enrich the adult HSC subset characterized by high-output and low-fitness signatures. To unbiasedly describe the model, we profiled tdTom+ and tdTom− LSK (Lin−c-Kit+Sca-1+) and LKs (Lin−c-Kit+ Sca1−) from young Flt3-Cre;LSL-tdTom mice (Figures 3A and 3B left). We observed that tdTom+ cells populated most clusters, including HSCs. Meanwhile, rare tdTom− cells were almost exclusively restricted to HSC and MkP clusters, suggesting a cell trajectory that indicates direct differentiation toward Mk, similar to the reported Mk-restricted pathway (Figures 3C and S3A–S3C) and a recent report using a similar model.<sup>25,41,45–49</sup> Approximately ~50% of E<sup>hi</sup>-SLAM HSCs (~80% of SLAM HSCs) were labeled tdTom+ at 8–12 weeks of age, suggesting that the Flt3-Cre tdTom model allows the separation of the Mk-restricted and non-Mk-restricted hierarchies (Figure 3D). We next performed differential gene expression analysis comparing tdTom+ and tdTom− HSCs (Figure 3E). We found that tdTom+ cells showed relative downregulation of stemness-associated genes like *Mecom* and positive enrichment for low-fitness and high-output signatures, as well

as inflammatory pathways, including IFN $\alpha$  and IL6/JAK/STAT3 signaling (Figure 3F). Thus, Flt3-Cre tdTom+ HSCs transcriptionally resemble low-fitness HSCs, with hallmarks of inflammatory priming and fast activation response.

To test the functional consequences of acquiring Dnmt3a R878H mutations in Flt3-Cre;tdTom+ HSCs, we generated Flt3-Cre; LSL-TdTomato; Dnmt3a-fl-R878H/+ mice and verified the specific and robust mutagenesis in this tdTom+ HSC population by genotyping PCR (Figure S3D). Next, we compared the single-cell transcriptional landscape of R878H tdTom+ with WT tdTom+ hematopoiesis (Figure 3B). We observed a relative loss of myeloid cells and expansion of erythroid progenitors in the R878H, in line with previous observations, suggesting this phenotype can arise without acquisition of the Dnmt3a mutation in the high-fitness HSCs (Figure S3E).<sup>50,51</sup> We then subsetted and reclustered tdTom+ HSCs. R878H tdTom+ cells were relatively enriched in cluster c0, which expresses higher levels of stemness regulators and quiescence-associated genes (Figures 3G and 3H). In line with this, R878H tdTom+ HSCs showed upregulation of stemness genes compared with WT tdTom+ HSCs (*Hlf* and *Mecom*), and GSEA showed positive enrichment of low-output, self-renewal, and high-fitness signatures, suggesting that R878H can enhance the stemness of tdTom+ HSCs *in vivo* (Figures 3I and 3J). Finally, we mixed 500 Flt3-Cre tdTom+ HSCs (R878H or wt) with 500 (age-matched) bulk CD45.1 HSCs in competitive *ex vivo* expansion cultures (Figure 3K). WT tdTom+ HSCs were quickly outcompeted, confirming the success of the Flt3-Cre system for enriching true low-fitness HSCs. By comparison, R878H HSCs showed a ~2-fold increased expansion, supporting that R878H can increase the fitness of tdTom+ HSCs (Figure 3L). Altogether, these results support our findings in clonally traced *ex vivo* cultures, and they demonstrate that Dnmt3a-R878H mutations can be acquired *in vivo* within the low-fitness HSC population (which represent ~80% of SLAM HSCs) and this is sufficient to reprogram their transcriptional state and competitive behavior. Considering the inflammatory priming signatures observed in tdTom+ HSCs and the reduced expression of early-response genes in R878H HSCs (e.g., *Jun*), we next hypothesized whether R878H was mediating its effects through protecting HSCs from inflammatory cues. To test this, we stimulated competitive *ex vivo* expanding cultures with IL1 $\beta$ , which drives HSC exhaustion through activation of myeloid differentiation (Figure 3M). Interestingly, in these inflammatory cultures, R878H tdTom+ HSCs showed increased competitive fitness, although they

(G) UMAP of subsetted HSCs showing the distribution density. The dotted line marks the border between cluster 0 (higher stemness markers) and clusters 1 and 2 (higher cell cycle and inflammatory response). Color scale is the UMAP density.

(H) Barplot showing relative enrichment ratio in cluster 0 versus clusters 1 and 2 for Flt3-Cre tdTom+ R878H-mutant versus Flt3-Cre tdTom+ wild-type HSCs. Mean  $\pm$  SD  $n = 2$ .

(I) Volcano plot showing differential expression analysis of Flt3-Cre tdTom+ R878H-mutant versus Flt3-Cre tdTom+ wild-type HSCs.

(J) GSEA showing hallmarks and HSC signatures for Flt3-Cre tdTom+ R878H-mutant versus Flt3-Cre tdTom+ wild-type HSCs. Scale is  $\log_{10}$  FDR<sup>−1</sup>.

(K) Experimental design for CD45.1 competition experiment using *ex vivo* expansion cultures.

(L) Proportion of tdTom+ cells (all cells) at day 20 comparing Flt3-Cre tdTom+ R878H and wild-type competitors. Mean  $\pm$  SD  $n = 6$  cultures, \*\*\*\* $p < 0.001$ .

(M) Scheme to evaluate effect of transient IL1 $\beta$  pulse in the fitness of various HSCs derived from different compartments. Competitor CD45.2 HSCs were sorted into the same well at 1:1 proportion with CD45.1 HSCs. After 72 h, media was replaced with expansion media containing 1 ng/ml IL1 $\beta$ . After 24 h, cells were washed twice with standard expansion media and continued to grow for an additional 15 days before flow cytometry analysis.

(N) Percentage of CD45.2+ cells at day 15 post IL1 $\beta$  washout. Competitor cells analyzed are Flt3-Cre tdTom−, Flt3-Cre tdTom+ (WT), and Flt3-Cre tdTom+ (R878H mutant).  $n = 5$  cultures per condition. Mean  $\pm$  SD \*\*\*\* $p < 0.001$ , \*\*\* $p < 0.005$ .

See also Tables S1, S2, S3, and S4.

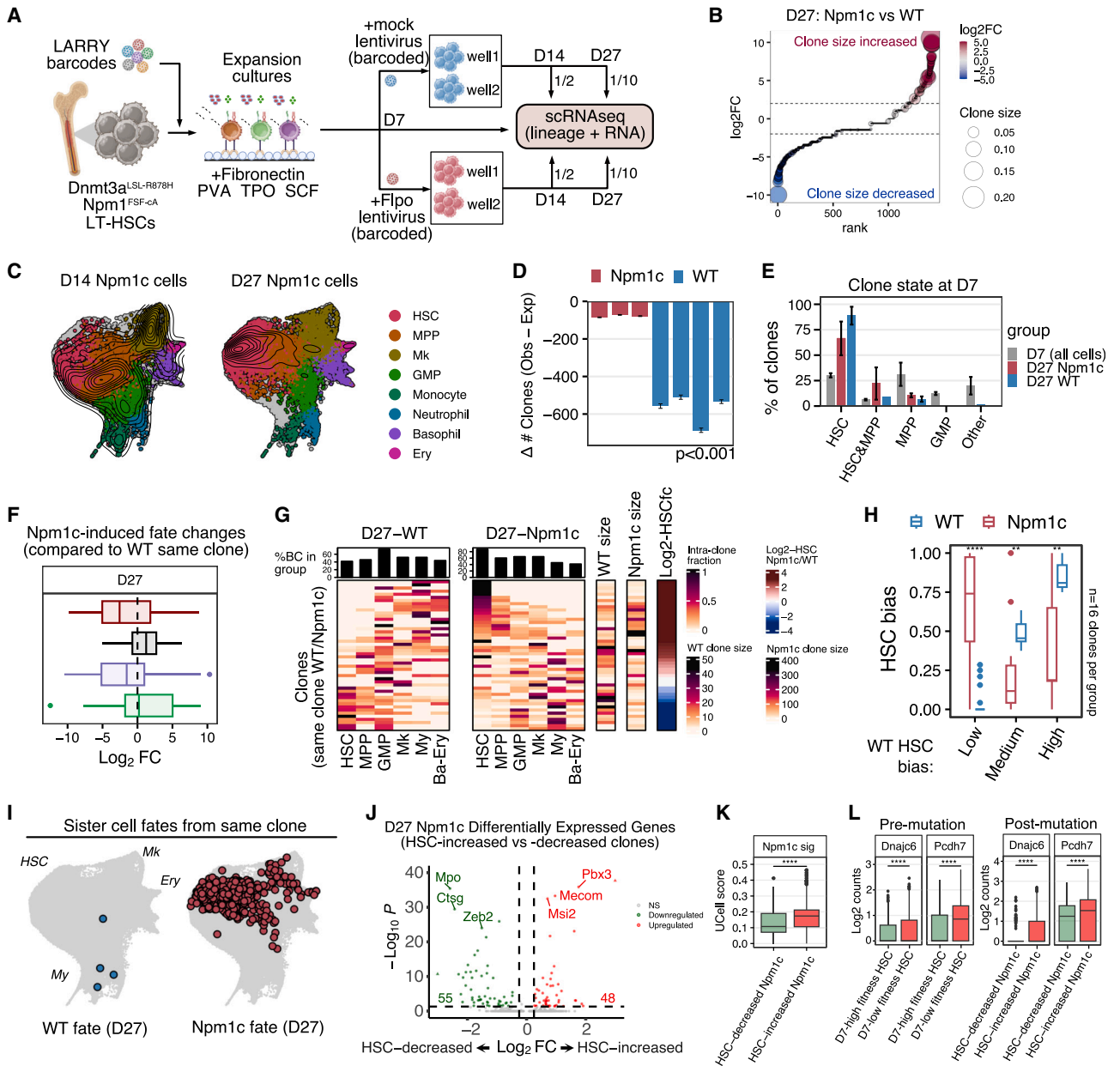


**Figure 4. Pre-existing stem cell states-fates determine unique properties in malignant Npm1c clones**

- (A) Experimental design for sister-cell state-fate analysis in Npm1c mutagenesis.  
 (B) Waterfall plot showing log<sub>2</sub> fold-change in clone size for the same set of clones with and without the Npm1c mutation.  
 (C) Integrated UMAP showing Npm1c mutant cells (all clones combined) at day 14 and day 27, colored by cluster groups.  
 (D) Difference between observed and expected number of clones at day 27, based on a stochastic sampling model.  
 (E) Barplot showing distribution of day 7 states for clones observed at day 27 (shown separately for WT or Npm1c). All day 7 states are shown for comparison.  
 (F) Boxplot showing sister clonal behavior changes at day 27. Data are expressed as log<sub>2</sub> fold-change (Npm1c versus WT) in the indicated measurement (for all clones observed at day 27 in both Npm1c and WT cultures, n = 48).  
 (G) State-bias heatmap of sister clones observed in both WT (mock) and Npm1c cultures at day 27 (n = 48). Rows are aligned (same clone in each line) across all columns and ranked according to HSC log fold-change. Additional columns show, for every clone, clonal proportion (size) in each culture and log<sub>2</sub> fold-change in HSC bias (Npm1c over WT).  
 (H) Boxplot showing the changes in HSC bias comparing the Npm1c and WT sister clones after separating them into 3 quantiles (low, medium, high), based on the HSC bias of the sister WT clones. n = 16 clones per group, ranked by WT output activity, \*\*\*\*p < 0.001, \*\*p < 0.01.  
 (I) Example UMAP of sister-cell wild-type and mutant fates at day 27 for a single clone.  
 (J) Volcano plot results of differential gene expression analysis comparing Npm1c clones with HSC-increased versus Npm1c clones with HSC-decreased. Example markers are highlighted.

(legend continued on next page)

remained less fit compared with more intrinsically resistant tdTom<sup>+</sup> HSCs (Figure 3N). Together, these results suggest that R878H at least partly mediates its fitness driver effects through protecting activation-primed HSCs from inflammatory-based exhaustion.

### Pre-existing stem cell states give rise to distinct malignant phenotypes upon Npm1c mutagenesis

Npm1c mutations are another frequent initiating alteration in AML and have been shown to endow stemness potential to mutant cells.<sup>52–54</sup> To investigate the effects of Npm1c at clonal resolution, we developed a third set of lentiviral libraries constitutively expressing GFP alongside Flpo recombinase or alone, and we then performed STRACK using the same mouse model, which carried a Flpo-inducible Npm1c allele (Figure 4A). As with Dnmt3a, we again observed a very heterogeneous but significant expansion of Npm1c mutant cells in competitive *ex vivo* expansion cultures (Figures 4B and S4A). This expansion was accompanied by the enrichment of Npm1c cells in an HSC-like state, which became conspicuous only at day 27, 20 days post-mutation (Figures 4C, S4B, and S4C). Compared to WT cultures, Npm1c cultures maintained almost perfect clonality, losing less than 25% of the clones expected based on the stochastic sampling model (Figure 4D). Based on prior findings, we speculated that contribution from non-HSC clones (e.g., GMPs) could explain these results, but tracing back the sister-cell states of these clones at day 7 confirmed that most clones still originated in HSCs (Figure 4E). Based on our experience with Dnmt3a, we decided to classify HSCs as Npm1c-independent or -dependent and compared their origins at day 7. Npm1c-dependent HSCs showed a low fitness score at day 7, which became reversed at day 27, highlighting the potent fitness-programming effect of the Npm1c mutation (Figure S4D). Npm1c mutant cells showed expected gene expression changes compared with WT cells, including increased expression of HoxA cluster genes, proteasome and ribosomal components, and stemness markers (Figures S4E–S4I; Table S3).

To quantify clonal changes in fate behaviors in response to Npm1c mutagenesis, we compared sister-cell clones that had been profiled in both WT and Npm1c cultures at day 27 (Figures 4F and 4G). We noticed that Npm1c mutation tended to expand HSCs and reduce output activity and My bias, but this was highly variable across clones. Surprisingly, sister clones with low-output and high HSC content in the WT setting displayed more mature states and decreased the proportion of HSC-like cells after acquiring the Npm1c mutation. Conversely, sister clones with high-output properties in the WT showed the most primitive and differentiation-blocked behaviors in the context of the Npm1c mutation (Figures 4H and S4J). This response was highly heritable, with independently mutated sisters of the original WT clone displaying similar behavior (Figure S4K). We next compared the gene expression profiles of clones that became more mature with Npm1c mutation

(“HSC-decreased”) with clones that became more primitive (“HSC-increased”) (Figure 4I; Table S3). HSC-decreased Npm1c clones expressed higher levels of mature malignant cell markers, including GMP genes (*Plac8* and *Mpo*) as well as various genes involved in AML function (*Zeb2* and *Plzf*),<sup>55,56</sup> whereas HSC-increased clones showed higher expression of canonical leukemic stemness genes (*Mecom* and *Msi2*) and higher expression of Npm1c Hox program genes (*Pbx3* and *Hoxa cluster*) (Figure 4J). Intriguingly, HSC-increased malignant clones still maintained expression of certain markers of their pre-mutant states such as *Pcdh7* or *Dnajc6*, which are part of the low-fitness HSC signature (Figure 4K). Comparing Npm1c clonal signatures based on the fitness score of their HSC of origin (at day 7) further confirmed these observations (Figure S4M). Finally, we evaluated clone-of-origin Npm1c signatures in published datasets of human AML samples that were previously classified as “mature” or “primitive” across two different cohorts, including bulk and scRNA-seq data.<sup>57,58</sup> We observed that Npm1c clonal signatures were recapitulated in different classes of AML patients, indicating that differences in HSC origins can drive malignant phenotypic heterogeneity that models relevant aspects of human leukemias (Figure S4N). Taken together, these results suggest that Npm1c mutations in low-fitness HSCs can generate more primitive malignant cell phenotypes, contrary to our expectations.

### Low-fitness HSCs give rise to primitive Npm1c malignant states *in vivo*

We next sought to validate the phenotypic differences observed across Npm1c clones using an *in vivo* assay. Since the Flt3-Cre;LSL-TdTomato model allows us to separate HSCs enriched in either high- or low-fitness signatures (Figure 3F), we crossed this model with the Flpo-inducible Npm1<sup>FSF-cA</sup> to study the consequences of the mutation in each HSC state. We sorted tdTom<sup>+</sup> or tdTom<sup>−</sup> HSCs and immediately transduced them with the Flpo-EGFP lentiviral library (Figure 5A). As expected, WT cultures derived from tdTom<sup>+</sup> HSCs quickly lost HSCs compared with tdTom<sup>−</sup>, and, while Npm1c mutation induced a relative gain of HSCs across both subsets, it did so to a greater extent in tdTom<sup>+</sup> cultures (Figure 5B). This suggests that the Flt3-Cre model allows us to partially enrich the clones that tend to lose HSCs with time (tdTom<sup>+</sup>) and increase their HSCs with Npm1c mutation.

To generate separate *in vivo* models, we transplanted tdTom<sup>−</sup> or tdTom<sup>+</sup> derived Npm1c cultures in sublethally irradiated recipient mice (Figure 5C). These mice inevitably progressed to a myeloid-dominant disease with expansion of Npm1c cells. Malignant cells derived from tdTom<sup>−</sup> HSCs expanded noticeably more than tdTom<sup>+</sup> derived Npm1c cells (Figure 5D), indicating a higher proliferation. By contrast, tdTom<sup>+</sup> Npm1c cells showed reduced output and a larger fraction CD48<sup>low</sup> HSPCs, in line with a more primitive, low-output phenotype (Figure 5E). Single-cell RNA-seq profiling confirmed our suspicions, with tdTom<sup>+</sup> Npm1c HSPCs showing a 2-fold increase in the number of cells

(K) Boxplot showing UCell score for the Npm1c-targets signature (*Hox*, *Pbx*, and *Meis* genes—see STAR Methods) across clones that lost HSCs upon Npm1c mutation (HSC-decreased,  $n = 261$ ) and acquired HSCs (HSC-increased,  $n = 3,032$ ) groups. \*\*\*\* $p < 0.001$ .

(L) Boxplot showing expression for two low-fitness marker genes (*Dnajc6* and *Pcdh7*) that show higher gene expression in low-fitness ( $n = 1,504$ ) and high-fitness ( $n = 345$ ) HSCs (pre-mutation, day 7) and HSC-increased ( $n = 3,032$ ) or -decreased ( $n = 261$ ) Npm1c clones (post-mutation, day 27).\*\*\*\* $p < 0.001$ . See also Tables S1, S2, S3, and S4.

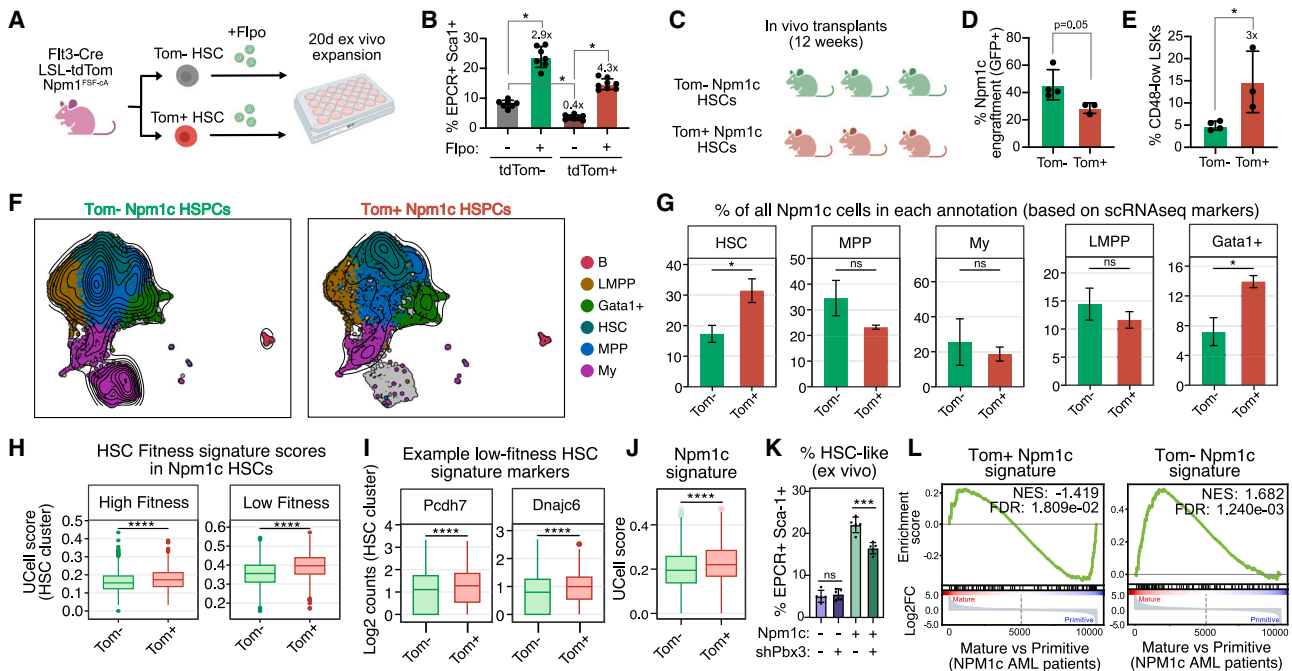


**Figure 5. Pre-existing states drive differences in Npm1c leukemic phenotypes *in vivo***

(A) Experimental design for studying Npm1c mutagenesis in Flt3-Cre tdTom+ versus tdTom- HSCs.  
 (B) Flow cytometry quantification of EPCR+ Sca-1+ (HSC-like) cells in WT and Npm1c mutant cells derived from either Flt3-Cre tdTom+ or tdTom- HSCs. Fold-change HSC expansion is indicated for each comparison. Mean  $\pm$  SD,  $n = 7$  and 8 cultures,  $*p < 0.05$ .  
 (C) *In vivo* transplant models of Flt3-Cre tdTom+ and tdTom- HSC-derived Npm1c malignancies.  
 (D) Flow cytometry quantification of total BM engraftment comparing tdTom+ and tdTom- HSC-derived Npm1c malignancies. Mean  $\pm$  SD,  $n = 4$  mice (tdTom-) and 3 mice (tdTom+),  $*p < 0.05$ .  
 (E) Flow cytometry quantification of CD48<sup>low</sup> LSKs in tdTom+ and tdTom- HSC-derived Npm1c malignancies.  
 (F) UMAP of scRNA-seq analyses comparing tdTom+ and tdTom- derived Npm1c malignancies (all mice per condition pooled). Cells are colored based on their clusters of origin. A density map overlay is shown.  
 (G) Barplot showing distribution of malignant states for tdTom- and tdTom+ derived Npm1c HSPCs. Mean  $\pm$  SD,  $n = 4$  mice (tdTom-) and 3 mice (tdTom+),  $*p < 0.05$ , ns: non-significant.  
 (H) Boxplot showing UCell HSC fitness signature scores for tdTom+ ( $n = 1,073$ ) and tdTom- ( $n = 1,094$ ) derived Npm1c malignant cells (comparing cells from the HSC cluster).  $****p < 0.001$ .  
 (I) Boxplot showing expression of example low-fitness signature genes comparing tdTom+ ( $n = 1,073$ ) and tdTom- ( $n = 1,094$ ) derived Npm1c cells.  $****p < 0.001$ .  
 (J) Boxplot showing the UCell Npm1c program signature score in the HSC cluster, comparing tdTom+ ( $n = 1,073$ ) and tdTom- ( $n = 1,094$ ) derived Npm1c cells.  $****p < 0.001$ .  
 (K) Percentage of HSC-like cells in Npm1c *ex vivo* cultures treated with Pbx3 shRNA. Mean  $\pm$  SD,  $n = 5$  cultures per condition,  $***p < 0.01$ , ns, not significant.  
 (L) GSEA of tdTom+ and tdTom- Npm1c-mutant bulk signatures in NPM1 AML patient samples grouped based on bulk-RNA-seq analysis (Mer et al. <sup>57</sup>). NES, normalized enrichment score; FDR, false discovery rate (FDR).  
 See also Tables S1, S2, S3, and S4.

annotated as “HSCs” compared with tdTom- Npm1c HSPCs (Figures 5F and 5G). Npm1c HSCs displayed certain markers of native HSCs (*Procr* and *Hlf*) and were more quiescent relative to other clusters but were fully depleted of CD150 (*Slamf1*) (Figures S5A–S5C and Table S3). Using the Flpo barcodes to identify clones, we further verified that the more primitive-like phenotype of tdTom+ Npm1c was due to the massive expansion of low-output (HSC-biased) clones (Figures S5D–S5F). Interestingly, the tdTom+ Npm1c HSCs showed higher expression of low-fitness signature genes compared with tdTom-, which might be explained by a gene expression memory from their ancestral pre-mutant HSC state, in line with our observations in *ex vivo* cultures (Figures 5H and 5I). Also consistent with the *ex vivo* results, tdTom+ Npm1c cells *in vivo* showed higher expression levels across most Npm1c-target genes (*Hoxa* cluster,

*Hoxb* cluster, *Pbx1*, *Pbx3*, and *Meis1*) (Figures 5J, S5H, and S5I).<sup>54</sup> This suggests that tdTom+ HSCs are more susceptible to Hox cluster activation upon Npm1c mutation, which can mechanistically explain the differences in differentiation block. To test whether abnormal hyperactivation of the Hox/Pbx/Meis signaling mediates HSC expansion, we silenced *Pbx3*, a key transcriptional mediator of Hox activity, and we observed reduced levels of EPCR+/Sca1+ cells in *ex vivo* Npm1c cultures (Figure 5K).<sup>59,60</sup> Thus, Npm1c-mediated hyperactivation of the Hox program is driving the expansion of the primitive phenotype. Together, our observations indicate that pre-existing HSC states can act as a non-genetic substrate for the activity of malignant mutations. We finally generated tdTom+ and tdTom- Npm1c gene signatures and performed GSEA on patient samples previously classified as mature or primitive, finding differential

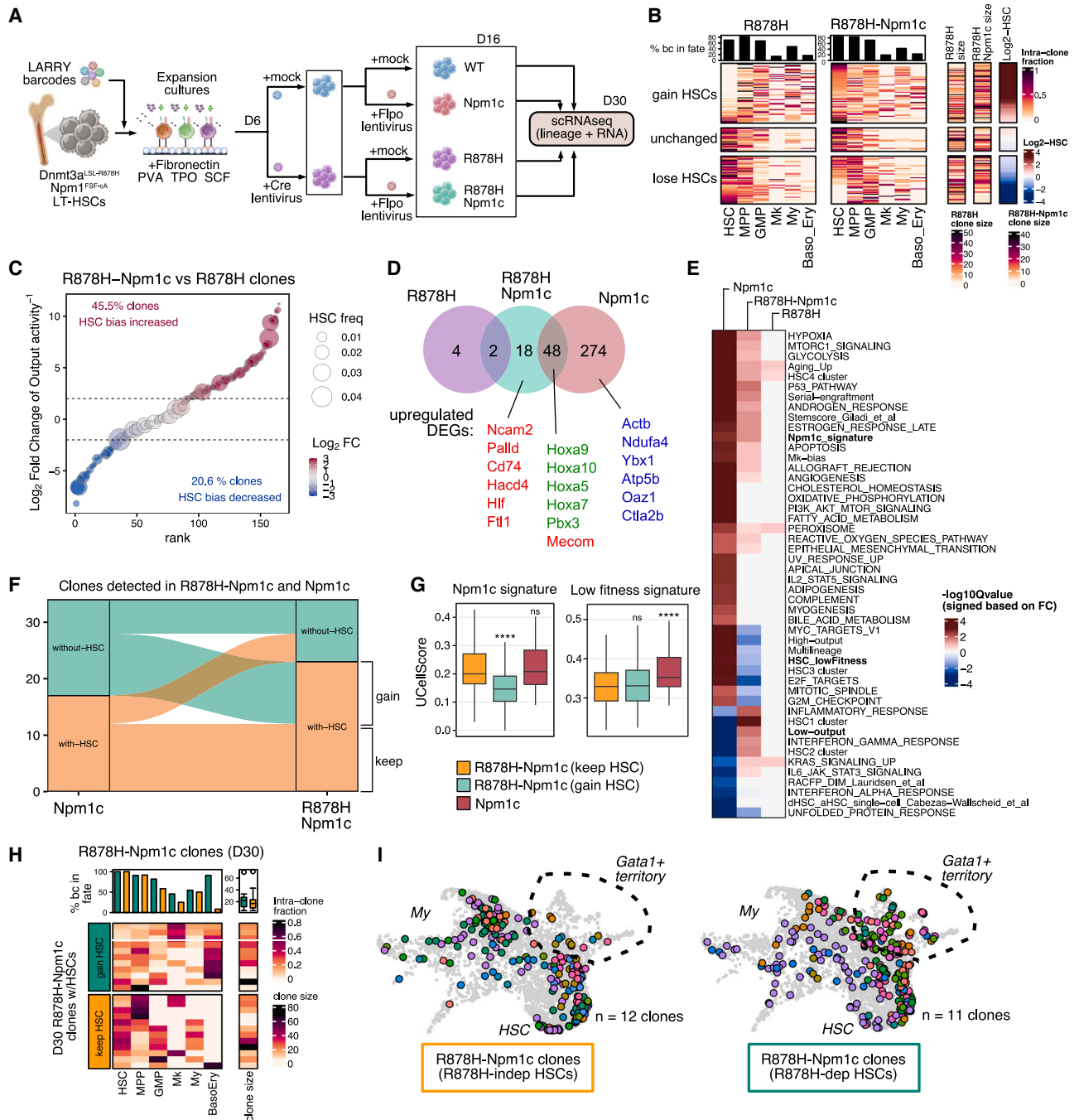


**Figure 6. Mutational synergism of *Dnmt3a*-R878H and *Npm1c* at the clonal level**

(A) Experimental design for sister-cell state-fate analysis in sequential *Dnmt3a* and *Npm1* mutagenesis.

(B) State-bias heatmap showing clones detected in both R878H and R878H/*Npm1c* double-mutant conditions at day 30. Rows are aligned (same clone in each line) across all columns and sorted based on change of HSC bias. Rows are separated in three blocks (gain, loss, or maintenance of HSCs, comparing double-mutant with R878H-only).

(C) Waterfall plot showing relative gain of HSC bias in R878H/*Npm1c* with respect to R878H-only condition. Scale indicates HSC bias change, from red (higher in R878H condition) to blue (higher in WT). Bubble size indicates the HSC frequency in the condition where it was highest.

(D) Venn diagram of differentially expressed genes (Wilcoxon test, log<sub>2</sub>FC > 0.25 and FDR < 0.05) in single and double-mutant HSCs with respect to mock control HSCs at day 30. Example relevant genes in each group are indicated and colored: green, *Npm1c* targets; red, low-output signature; blue, high-output signature.

(E) Heatmap showing *q* value results of single-cell pathway analysis (SCPA) comparing single- or double-mutant HSCs with respect to mock control HSCs at day 30. *q* value scale relates to the number of genes changed, and the *q* value sign indicates the direction of change (positive means enriched in mutant condition).

(F) Alluvial plot showing the proportion of clones that gain HSCs only with R878H/*Npm1c* mutation. *y* axis indicates the number of clones, and *x* axis represents the sample of origin.

(legend continued on next page)

enrichment of these signatures across patient groups (Figure 5L). Together these results suggest that the Flt3-Cre system can be used to separately model relevant aspects of NPM1 disease heterogeneity in humans.

### Sequential Dnmt3a-Npm1 mutagenesis reveals synergism and phenotypic shift

Approximately 60% of NPM1 leukemias acquire this AML-defining mutation in cells with a pre-existing lesion in DNMT3A. To decipher how the Dnmt3a mutant background impacts the effect of Npm1c-driven transformation at the clonal level, we designed an experiment for sequential acquisition of both mutations that still allowed us to sample a common set of clones across the four conditions (mock/WT, Npm1c, Dnmt3a, and Dnmt3a/Npm1c), profiling them by scRNA-seq at the last time point (day 30) (Figures 6A, S6A, and S6B).

We observed that double-mutant Dnmt3a/Npm1c cultures showed the highest percentage of clones that maintained HSCs (>60%) in our entire study, surpassing either single mutation (Figures S6C–S6E). Dnmt3a/Npm1c clones showed a further increase in HSC bias compared with the same clones with either single mutation (Figures 6B, 6C, and S6F). These results indicate a highly penetrant synergistic effect, with pre-existing Dnmt3a mutations preventing the exhaustion of Npm1 mutant clones from the HSC pool.

Next, to identify unique and shared gene programs, we performed gene expression analysis on HSCs across the four groups. As expected, both Dnmt3a/Npm1c and Npm1c-only HSCs showed upregulation of Npm1c signature genes (Hoxa cluster, Meis, Pbx), but Npm1c-only HSCs showed more pronounced dysregulation of the canonical HSC identity, with hallmarks of Myc, E2F, mTOR/ phosphatidylinositol 3-kinase (PI3K), and cell cycle activity (Figures 6D, 6E, S6F, and S6G). By contrast, Dnmt3a/Npm1c cells showed a relative suppression of these activation programs. Surprised by this finding, we next separated the clones that “gained” HSCs only with Dnmt3a as a background mutation from the clones that “maintained” HSCs independent of Dnmt3a. Dnmt3a-independent Npm1c HSCs showed equal levels of Hox activity as Npm1c-only and were strongly HSC-biased, indicating a minor advantage for a pre-existing Dnmt3a mutation in these cases (Figure 6G). By contrast, Dnmt3a-dependent Npm1c HSCs showed a reduced Hox-signature expression and a strong Gata1+ fate bias, in line with the effects of R878H, as observed before (Figures 6G–6I). Taken together, our observations clarify a synergistic role of Dnmt3a-R878H and Npm1c, which enables Gata1-lineage-biased R878H HSCs to self-renew and persist after acquiring an Npm1c mutation.

## DISCUSSION

Phenotypic heterogeneity (plasticity, memory, and noise) impacts critical therapeutic aspects of cancer, such as treatment

resistance and clonal dominance, which can be traced back to the non-genetic variation in individual cancer cells.<sup>61,62</sup> Our findings here suggest that pre-existing heterogeneity in the cells of origin can also be a source of phenotypic cancer heterogeneity, even upon acquisition of identical cancer driver mutations, and their study requires advanced single-cell tracing approaches to circumvent limitations of traditional approaches.<sup>24,29</sup> We propose that STRACK can empower a conceptual and methodological shift from the traditional cell-of-origin model to a more nuanced clone-of-origin paradigm, which takes into account both lineage and state information, as we have described for the two mutations in this study.

At the population level, we observed that the Dnmt3a R878H mutation (R882H in humans) enhances the fitness and expansion of HSCs, consistent with prior studies.<sup>34,37</sup> Also, R878H HSCs exhibited reduced inflammatory response hallmarks, in line with recent studies in zebrafish, mice, and human clonal hematopoiesis.<sup>38–40,63</sup> However, at the single-clone level, the R878H mutation showed a wide range of responses, with a more pronounced effect on low-fitness HSCs. These stem cells are primed to activate and differentiate quickly and normally get outcompeted by inflammation-protected high-fitness HSCs. Yet, upon R878H mutation, low-fitness HSCs significantly increased their self-renewal potential, and this was at least partially explained by a reduced responsiveness to inflammatory stimulation.

Similarly, the Npm1c mutation consistently activated Pbx/Hoxa cluster expression, in line with its well-described role in activating these stemness genes.<sup>52,54,64–66</sup> Yet, the individual clonal responses to this mutation varied greatly. Unexpectedly, low-fitness HSCs gave rise to more primitive malignant cells, with a bias toward stem-cell-like states. Previous studies in MLL-rearranged AML models have suggested that cancer cells inherit pre-existing functionalities of the cell of origin.<sup>14</sup> However, our Npm1c results completely upset the notion that these state biases are always maintained post mutation. Notably, our different Npm1c clones exhibited characteristics of various human AML LSC subtypes, which are increasingly recognized as a major source of therapy-response variability.<sup>67,68</sup>

Why do low-fitness HSCs respond in such a unique way to the Npm1c transforming mutation? Malignant cells derived from low-fitness clones showed increased activation of the Hox/Pbx/Meis program, which drove the expansion of HSC-like cells. This suggests that, although Npm1c is sufficient to activate this program, it is further modulated by specific pre-existing non-genetic determinants. Interestingly, a recent report also found a specific Hox positional gene program that interacts with oncogenic mutations to drive acral melanoma.<sup>6</sup> We speculate that anatomical origins (which can be highly diverse in the hematopoietic system) may also underlie the phenotypic differences that we report. Our finding that low-fitness HSCs are primed to respond to inflammatory insults also suggests that stem cell-activating events inscribed in the chromatin are being co-opted

(G) Boxplot showing UCell score of Npm1c signature (left) and low-fitness signature (right) comparing R878H/Npm1c HSCs separated based on whether they gain ( $n = 51$ ) or maintain HSCs ( $n = 72$ ) compared with the Npm1c-only ( $n = 44$ ) condition. \*\*\*\* $p < 0.001$ , ns: not significantly different.

(H) State-bias heatmap showing R878H/Npm1c clones that gain (green) or maintain (orange) HSCs with double mutation with respect to Npm1c only.

(I) UMAP showing the distribution of R878H-Npm1c clones, separated based on their R878H dependency to maintain HSCs. Cells are colored based on their clone of origin (randomly picking colors for visualization). The Gata1+ region of the UMAP is indicated with a dotted line.

See also Tables S1, S2, S3, and S4.

by Npm1c mutations. This resembles recent reports in pancreatic and skin cancer initiation, where inflammation has been linked to chromatin licensing events required for transformation by driver mutations.<sup>69–71</sup>

While we have not ruled out the contribution of pre-existing genetic diversity to our results, we believe this to be unlikely. It is well reported that mouse HSCs divide slowly, have a high diversity of developmental precursors at a young age, and have a low frequency of recurrent cancer driver mutations.<sup>72–74</sup> Though this supports a mostly non-genetic mechanism, this does not exclude the contribution of genetics and extrinsic factors, particularly in longer-lived human systems. Past work has elucidated the role of genetic predispositions<sup>75,76</sup> and extrinsic regulation in the expansion of initiating (pre)-malignant clones.<sup>53,63,77</sup> Based on all this evidence, we would like to propose here the concept of a ‘clonal reaction norm,’ where the clonal history—developmental origin, genetic background, sequence of driver mutations, and environmental factors—collectively determines the fate and properties of a cancer-initiating clone. Understanding these norms for different cancer driver genes may have a direct impact on diagnostics and personalized treatments.

Finally, we want to highlight that our experimental design should be amenable to other driver genes and systems beyond hematopoiesis. Looking ahead, we anticipate the development of mouse models that can reproducibly generate tumors from clone-specific origins, offering a more accurate representation of the non-genetic tumor diversity that characterizes human patients to advance precision medicine efforts.

### Limitations of the study

These studies have been performed using mice, due to the accessibility of precision mutagenesis that can be achieved using genetically engineered Cre/Flp-conditional mouse alleles. In the future, CRISPR-based precision editing might enable similar approaches in primary human HSCs.<sup>78</sup>

Our definition of “high fitness” or “low fitness” is not quantitative, and it is strictly based on our capacity to detect clones in expansion cultures at the last sampling time point (27–30 days). While fitness correlated with self-renewal (HSC numbers per clone), as expected, this may be specific to our experimental context.

We used *ex vivo* expansion cultures to maximize our capacity to maintain and track many stem cell clones longitudinally, in separate environments, with and without mutations, something that is difficult to achieve in a transplantation setting. Future technological implementations should address the role of the stem cell niche.<sup>79–81</sup>

Finally, our state-fate analysis relies on sister-cell splitting and clonal analysis, with sister states/fates serving as a proxy. Advanced technologies are emerging to allow same-cell tracing without destruction and may eventually have the throughput to perform STRACK-type studies at scale.<sup>82</sup>

### RESOURCE AVAILABILITY

#### Lead contact

Further information and requests for resources and reagents should be directed to and will be fulfilled by the lead contact, Alejo E. Rodríguez-Fraticelli, ([alejo.rodriguez-fraticelli@irbbarcelona.org](mailto:alejo.rodriguez-fraticelli@irbbarcelona.org)).

### Materials availability

Plasmids and plasmid libraries have been deposited and can be requested from Addgene.

### Data and code availability

- Raw and processed single-cell RNA-seq, LARRY barcoding, and TotalSeq™ library sequencing data have been deposited at GEO: GSE266232, GSE282755, and GSE282756, and are publicly available as of the date of publication. All original code has been deposited and is publicly available at Zenodo: <https://doi.org/10.5281/zenodo.14261507> as of the date of publication.
- Any additional information required to reanalyze the data reported in this paper is available from the [lead contact](#) upon request.

### ACKNOWLEDGMENTS

This work was supported by the Cris contra el Cáncer Foundation Excellence Award (PR\_EX\_2020-24), the European Commission’s Horizon Europe program, through the ERC Starting Grant MemOriStem (101042992), the Spanish National Research Agency (PID2020-114638RA-I00, PID2023-148073OB-I00), the Agencia de Gestio d’Ajuts Universitaris i de Recerca (2017 SGR 1322), and the CERCA Program/Generalitat de Catalunya. A.E.R.-F. acknowledges support from the Institut Català de Recerca i Estudis Avançats (ICREA) and past support from the Ministry of Science Ramon y Cajal Fellowship and the LaCaixa Junior Fellows Incoming Fellowship. I.S. was supported through the European Union’s Horizon 2020 research and innovation program under the Marie Skłodowska-Curie grant agreement no 945352. D.F.-P. was supported through the Marie Skłodowska-Curie grant agreement no 101109276. The authors would like to acknowledge the technical assistance of the Functional Genomics Core Facility at IRB Barcelona (single-cell library preparations and sequencing), the Flow Cytometry and Cell Sorting Facility at the University of Barcelona (CCIT-UB), and other facilities from IRB and the Parc Científic de Barcelona (PCB). The authors also wish to thank colleagues in the ISEH community, the Fraticelli lab, and IRB Barcelona for various helpful discussions. Illustrations were created with Biorender.

### AUTHOR CONTRIBUTIONS

A.E.R.-F., I.S., and D.F.-P. conceptualized the project design. I.S. performed molecular biology, library preparations, cell culture, and animal experiments. D.F.-P. generated the analytic pipelines and performed bioinformatic, single-cell sequencing, and statistical analyses and generated most figures. P.S.S. assisted in the generation of the bioinformatic pipeline and analysis. A.E.R.-F. designed the LARRY libraries. I.S. generated all the vectors and produced the lentiviral libraries with assistance from lab members. I.S. and D.F.-P. wrote the manuscript with assistance from A.E.R.-F. A.E.R.-F. supervised all aspects of the study.

### DECLARATION OF INTERESTS

A.E.R.-F. is an advisor for Retro Biosciences.

### STAR★METHODS

Detailed methods are provided in the online version of this paper and include the following:

- [KEY RESOURCES TABLE](#)
- [EXPERIMENTAL MODEL AND STUDY PARTICIPANT DETAILS](#)
  - Animals
  - Primary cell cultures
- [METHOD DETAILS](#)
  - Hematopoietic stem cell isolation
  - Construction of lentiviral pLARRY vectors
  - Barcode lentivirus library generation and diversity estimation
  - Single-cell encapsulation and library preparation for sequencing
  - scRNA-seq data processing and calling of lineage barcodes

- Single-cell integration, clustering and annotation
- **QUANTIFICATION AND STATISTICAL ANALYSIS**
- Quantification and classification of HSC clonal behaviors
- Sister cell similarity analysis
- Stochastic sampling model of clonal selection
- Single-cell differential gene expression and signature scores
- Gene set enrichment analysis
- Additional data visualization and figure preparation
- Statistical methods

### SUPPLEMENTAL INFORMATION

Supplemental information can be found online at <https://doi.org/10.1016/j.stem.2025.01.012>.

Received: May 4, 2024

Revised: December 2, 2024

Accepted: January 23, 2025

Published: February 25, 2025

### REFERENCES

1. Lenz, G., Onzi, G.R., Lenz, L.S., Buss, J.H., Dos Santos, J.A., and Beghini, K.R. (2022). The Origins of Phenotypic Heterogeneity in Cancer. *Cancer Res.* 82, 3–11. <https://doi.org/10.1158/0008-5472.CAN-21-1940>.
2. Blanpain, C. (2013). Tracing the cellular origin of cancer. *Nat. Cell Biol.* 15, 126–134. <https://doi.org/10.1038/ncb2657>.
3. Visvader, J.E. (2011). Cells of origin in cancer. *Nature* 469, 314–322. <https://doi.org/10.1038/nature09781>.
4. Baggiolini, A., Callahan, S.J., Montal, E., Weiss, J.M., Trieu, T., Tagore, M.M., Tischfield, S.E., Walsh, R.M., Suresh, S., Fan, Y., et al. (2021). Developmental chromatin programs determine oncogenic competence in melanoma. *Science* 373, eabc1048. <https://doi.org/10.1126/science.abc1048>.
5. Rajbhandari, N., Hamilton, M., Quintero, C.M., Ferguson, L.P., Fox, R., Schürch, C.M., Wang, J., Nakamura, M., Lytle, N.K., McDermott, M., et al. (2023). Single-cell mapping identifies MSI cells as a common origin for diverse subtypes of pancreatic cancer. *Cancer Cell* 41, 1989–2005.e9. <https://doi.org/10.1016/j.ccell.2023.09.008>.
6. Weiss, J.M., Hunter, M.V., Cruz, N.M., Baggiolini, A., Tagore, M., Ma, Y., Misale, S., Marasco, M., Simon-Vermot, T., Campbell, N.R., et al. (2022). Anatomic position determines oncogenic specificity in melanoma. *Nature* 604, 354–361. <https://doi.org/10.1038/s41586-022-04584-6>.
7. Krivtsov, A.V., Figueroa, M.E., Sinha, A.U., Stubbs, M.C., Feng, Z., Valk, P.J.M., Delwel, R., Döhner, K., Bullinger, L., Kung, A.L., et al. (2013). Cell of origin determines clinically relevant subtypes of MLL-rearranged AML. *Leukemia* 27, 852–860. <https://doi.org/10.1038/leu.2012.363>.
8. Cai, S.F., Chu, S.H., Goldberg, A.D., Parvin, S., Koche, R.P., Glass, J.L., Stein, E.M., Tallman, M.S., Sen, F., Famulare, C.A., et al. (2020). Leukemia Cell of Origin Influences Apoptotic Priming and Sensitivity to LSD1 Inhibition. *Cancer Discov.* 10, 1500–1513. <https://doi.org/10.1158/2159-8290.CD-19-1469>.
9. Zeisig, B.B., Fung, T.K., Zarowiecki, M., Tsai, C.T., Luo, H., Stanojevic, B., Lynn, C., Leung, A.Y.H., Zuna, J., Zalova, M., et al. (2021). Functional reconstruction of human AML reveals stem cell origin and vulnerability of treatment-resistant MLL-rearranged leukemia. *Sci. Transl. Med.* 13, eabc4822. <https://doi.org/10.1126/scitranslmed.abc4822>.
10. Taussig, D.C., Vargaftig, J., Miraki-Moud, F., Griessinger, E., Sharrock, K., Luke, T., Lillington, D., Oakervee, H., Cavenagh, J., Agrawal, S.G., et al. (2010). Leukemia-initiating cells from some acute myeloid leukemia patients with mutated nucleophosmin reside in the CD34(-) fraction. *Blood* 115, 1976–1984. <https://doi.org/10.1182/blood-2009-02-206565>.
11. Cozzio, A., Passegué, E., Ayton, P.M., Karsunky, H., Cleary, M.L., and Weissman, I.L. (2003). Similar MLL-associated leukemias arising from self-renewing stem cells and short-lived myeloid progenitors. *Genes Dev.* 17, 3029–3035. <https://doi.org/10.1101/gad.1143403>.
12. Huntly, B.J.P., Shigematsu, H., Deguchi, K., Lee, B.H., Mizuno, S., Duclos, N., Rowan, R., Amaral, S., Curley, D., Williams, I.R., et al. (2004). MOZ-TIF2, but not BCR-ABL, confers properties of leukemic stem cells to committed murine hematopoietic progenitors. *Cancer Cell* 6, 587–596. <https://doi.org/10.1016/j.ccr.2004.10.015>.
13. Krivtsov, A.V., Twomey, D., Feng, Z., Stubbs, M.C., Wang, Y., Faber, J., Levine, J.E., Wang, J., Hahn, W.C., Gilliland, D.G., et al. (2006). Transformation from committed progenitor to leukaemia stem cell initiated by MLL-AF9. *Nature* 442, 818–822. <https://doi.org/10.1038/nature04980>.
14. George, J., Uyar, A., Young, K., Kuffler, L., Waldron-Francis, K., Marquez, E., Ucar, D., and Trowbridge, J.J. (2016). Leukaemia cell of origin identified by chromatin landscape of bulk tumour cells. *Nat. Commun.* 7, 12166. <https://doi.org/10.1038/ncomms12166>.
15. SanMiguel, J.M., Eudy, E., Loberg, M.A., Miles, L.A., Stearns, T., Mistry, J.J., Rauh, M.J., Levine, R.L., and Trowbridge, J.J. (2022). Cell origin-dependent cooperativity of mutant Dnmt3a and Npm1 in clonal hematopoiesis and myeloid malignancy. *Blood Adv.* 6, 3666–3677. <https://doi.org/10.1182/bloodadvances.2022006968>.
16. Stavropoulou, V., Kaspar, S., Brault, L., Sanders, M.A., Juge, S., Moretini, S., Tzankov, A., Iacovino, M., Lau, I.-J., Milne, T.A., et al. (2016). MLL-AF9 Expression in Hematopoietic Stem Cells Drives a Highly Invasive AML Expressing EMT-Related Genes Linked to Poor Outcome. *Cancer Cell* 30, 43–58. <https://doi.org/10.1016/j.ccell.2016.05.011>.
17. Paul, F., Arkin, Y., 'ara, Giladi, A., Jaitin, D.A., Kenigsberg, E., Keren-Shaul, H., Winter, D., Lara-Astiaso, D., Gury, M., Weiner, A., et al. (2016). Transcriptional Heterogeneity and Lineage Commitment in Myeloid Progenitors. *Cell* 164, 325.
18. Giladi, A., Paul, F., Herzog, Y., Lubling, Y., Weiner, A., Yofe, I., Jaitin, D., Cabezas-Wallscheid, N., Dress, R., Ginhoux, F., et al. (2018). Single-cell characterization of haematopoietic progenitors and their trajectories in homeostasis and perturbed haematopoiesis. *Nat. Cell Biol.* 20, 836–846. <https://doi.org/10.1038/s41556-018-0121-4>.
19. Li, L., Bowling, S., McGeary, S.E., Yu, Q., Lemke, B., Alcedo, K., Jia, Y., Liu, X., Ferreira, M., Klein, A.M., et al. (2023). A mouse model with high clonal barcode diversity for joint lineage, transcriptomic, and epigenomic profiling in single cells. *Cell* 186, 5183–5199.e22. <https://doi.org/10.1016/j.cell.2023.09.019>.
20. Jindal, K., Adil, M.T., Yamaguchi, N., Yang, X., Wang, H.C., Kamimoto, K., Rivera-Gonzalez, G.C., and Morris, S.A. (2024). Single-cell lineage capture across genomic modalities with CellTag-multi reveals fate-specific gene regulatory changes. *Nat. Biotechnol.* 42, 946–959. <https://doi.org/10.1038/s41587-023-01931-4>.
21. Perié, L., Duffy, K.R., Kok, L., de Boer, R.J., and Schumacher, T.N. (2015). The Branching Point in Erythro-Myeloid Differentiation. *Cell* 163, 1655–1662. <https://doi.org/10.1016/j.cell.2015.11.059>.
22. Wang, S.-W., Herriges, M.J., Hurley, K., Kotton, D.N., and Klein, A.M. (2022). CoSpar identifies early cell fate biases from single-cell transcriptomic and lineage information. *Nat. Biotechnol.* 40, 1066–1074. <https://doi.org/10.1038/s41587-022-01209-1>.
23. Wagner, D.E., and Klein, A.M. (2020). Lineage tracing meets single-cell omics: opportunities and challenges. *Nat. Rev. Genet.* 21, 410–427. <https://doi.org/10.1038/s41576-020-0223-2>.
24. Weinreb, C., Rodríguez-Fraticelli, A., Camargo, F.D., and Klein, A.M. (2020). Lineage tracing on transcriptional landscapes links state to fate during differentiation. *Science* 367, eaaw3381. <https://doi.org/10.1126/science.aaw3381>.
25. Rodríguez-Fraticelli, A.E., Wolock, S.L., Weinreb, C.S., Panero, R., Patel, S.H., Jankovic, M., Sun, J., Calogero, R.A., Klein, A.M., and Camargo, F.D. (2018). Clonal analysis of lineage fate in native haematopoiesis. *Nature* 553, 212–216. <https://doi.org/10.1038/nature25168>.
26. Naik, S.H., Perié, L., Swart, E., Gerlach, C., van Rooij, N., de Boer, R.J., and Schumacher, T.N. (2013). Diverse and heritable lineage imprinting of early haematopoietic progenitors. *Nature* 499, 229–232. <https://doi.org/10.1038/nature12013>.

27. Dykstra, B., Kent, D., Bowie, M., McCaffrey, L., Hamilton, M., Lyons, K., Lee, S.-J., Brinkman, R., and Eaves, C. (2007). Long-term propagation of distinct hematopoietic differentiation programs in vivo. *Cell Stem Cell* 7, 218–229. <https://doi.org/10.1016/j.stem.2007.05.015>.
28. Wilson, N.K., Kent, D.G., Buettner, F., Shehata, M., Macaulay, I.C., Calero-Nieto, F.J., Sánchez Castillo, M., Oedekoven, C.A., Diamanti, E., Schulte, R., et al. (2015). Combined Single-Cell Functional and Gene Expression Analysis Resolves Heterogeneity within Stem Cell Populations. *Cell Stem Cell* 16, 712–724. <https://doi.org/10.1016/j.stem.2015.04.004>.
29. Tian, L., Tomei, S., Schreuder, J., Weber, T.S., Amann-Zalcenstein, D., Lin, D.S., Tran, J., Audiger, C., Chu, M., Jarratt, A., et al. (2021). Clonal multi-omics reveals Bcor as a negative regulator of emergency dendritic cell development. *Immunity* 54, 1338–1351.e9. <https://doi.org/10.1016/j.immuni.2021.03.012>.
30. Haas, S., Trumpp, A., and Milsom, M.D. (2018). Causes and Consequences of Hematopoietic Stem Cell Heterogeneity. *Cell Stem Cell* 22, 627–638. <https://doi.org/10.1016/j.stem.2018.04.003>.
31. Tong, J., Sun, T., Ma, S., Zhao, Y., Ju, M., Gao, Y., Zhu, P., Tan, P., Fu, R., Zhang, A., et al. (2021). Hematopoietic stem cell heterogeneity is linked to the initiation and therapeutic response of myeloproliferative neoplasms. *Cell Stem Cell* 28, 780. <https://doi.org/10.1016/j.stem.2021.02.026>.
32. Wilkinson, A.C., Ishida, R., Kikuchi, M., Sudo, K., Morita, M., Crisostomo, R.V., Yamamoto, R., Loh, K.M., Nakamura, Y., Watanabe, M., et al. (2019). Long-term ex vivo haematopoietic-stem-cell expansion allows nonconditioned transplantation. *Nature* 571, 117–121. <https://doi.org/10.1038/s41586-019-1244-x>.
33. Che, J.L.C., Bode, D., Kucinski, I., Cull, A.H., Bain, F., Becker, H.J., Jassinskaja, M., Barile, M., Boyd, G., Belmonte, M., et al. (2022). Identification and characterization of in vitro expanded hematopoietic stem cells. *EMBO Rep.* 23, e55502. <https://doi.org/10.15252/embr.202255502>.
34. Loberg, M.A., Bell, R.K., Goodwin, L.O., Eudy, E., Miles, L.A., SanMiguel, J.M., Young, K., Bergstrom, D.E., Levine, R.L., Schneider, R.K., et al. (2019). Sequentially inducible mouse models reveal that Npm1 mutation causes malignant transformation of Dnmt3a-mutant clonal hematopoiesis. *Leukemia* 33, 1635–1649. <https://doi.org/10.1038/s41375-018-0368-6>.
35. Zhang, Q., Olofzon, R., Konturek-Ciesla, A., Yuan, O., and Bryder, D. (2024). Ex vivo expansion potential of murine hematopoietic stem cells is a rare property only partially predicted by phenotype. *eLife* 12, RP91826. <https://doi.org/10.7554/eLife.91826>.
36. Rodriguez-Fraticelli, A.E., Weinreb, C., Wang, S.-W., Migueles, R.P., Jankovic, M., Usart, M., Klein, A.M., Lowell, S., and Camargo, F.D. (2020). Single-cell lineage tracing unveils a role for TCF15 in haematopoiesis. *Nature* 583, 585–589. <https://doi.org/10.1038/s41586-020-2503-6>.
37. Guryanova, O.A., Shank, K., Spitzer, B., Luciani, L., Koche, R.P., Garrett-Bakelman, F.E., Ganzel, C., Durham, B.H., Mohanty, A., Hoermann, G., et al. (2016). DNMT3A mutations promote anthracycline resistance in acute myeloid leukemia via impaired nucleosome remodeling. *Nat. Med.* 22, 1488–1495. <https://doi.org/10.1038/nm.4210>.
38. Jakobsen, N.A., Turkalj, S., Zeng, A.G.X., Stoilova, B., Metzner, M., Nagree, M.S., Shah, S., Moore, R., Usukhbayer, B., Salazar, M.A., et al. (2023). Selective advantage of mutant stem cells in clonal hematopoiesis occurs by attenuating the deleterious effects of inflammation and aging. Preprint at bioRxiv. <https://doi.org/10.1101/2023.09.12.557322>.
39. Avagyan, S., and Zon, L.I. (2023). Clonal hematopoiesis and inflammation—the perpetual cycle. *Trends Cell Biol.* 33, 695–707. <https://doi.org/10.1016/j.tcb.2022.12.001>.
40. Avagyan, S., Henninger, J.E., Mannherz, W.P., Mistry, M., Yoon, J., Yang, S., Weber, M.C., Moore, J.L., and Zon, L.I. (2021). Resistance to inflammation underlies enhanced fitness in clonal hematopoiesis. *Science* 374, 768–772. <https://doi.org/10.1126/science.aba9304>.
41. Meng, Y., Carrelha, J., Drissen, R., Ren, X., Zhang, B., Gambardella, A., Valletta, S., Thongjuea, S., Jacobsen, S.E., and Nerlov, C. (2023). Epigenetic programming defines haematopoietic stem cell fate restriction. *Nat. Cell Biol.* 25, 812–822. <https://doi.org/10.1038/s41556-023-01137-5>.
42. Buza-Vidas, N., Woll, P., Hultquist, A., Duarte, S., Lutteropp, M., Bouriez-Jones, T., Ferry, H., Luc, S., and Jacobsen, S.E.W. (2011). FLT3 expression initiates in fully multipotent mouse hematopoietic progenitor cells. *Blood* 118, 1544–1548. <https://doi.org/10.1182/blood-2010-10-316232>.
43. Beaudin, A.E., Boyer, S.W., Perez-Cunningham, J., Hernandez, G.E., Derderian, S.C., Jujavarapu, C., Aaserude, E., MacKenzie, T., and Forsberg, E.C. (2016). A Transient Developmental Hematopoietic Stem Cell Gives Rise to Innate-like B and T Cells. *Cell Stem Cell* 19, 768–783. <https://doi.org/10.1016/j.stem.2016.08.013>.
44. Stonehouse, O.J., Biben, C., Weber, T.S., Garnham, A., Fennell, K.A., Farley, A., Terreaux, A.F., Alexander, W.S., Dawson, M.A., Naik, S.H., et al. (2024). Clonal analysis of fetal hematopoietic stem/progenitor cell subsets reveals how post-transplantation capabilities are distributed. Preprint at bioRxiv. <https://doi.org/10.1101/2024.02.19.579920>.
45. Haas, S., Hansson, J., Klimmeck, D., Loeffler, D., Velten, L., Uckelmann, H., Wurzer, S., Prendergast, Á.M., Schnell, A., Hexel, K., et al. (2015). Inflammation-Induced Emergency Megakaryopoiesis Driven by Hematopoietic Stem Cell-like Megakaryocyte Progenitors. *Cell Stem Cell* 17, 422–434. <https://doi.org/10.1016/j.stem.2015.07.007>.
46. Yamamoto, R., Wilkinson, A.C., Oeohara, J., Lan, X., Lai, C.-Y., Nakauchi, Y., Pritchard, J.K., and Nakauchi, H. (2018). Large-Scale Clonal Analysis Resolves Aging of the Mouse Hematopoietic Stem Cell Compartment. *Cell Stem Cell* 22, 600–607.e4. <https://doi.org/10.1016/j.stem.2018.03.013>.
47. Carrelha, J., Meng, Y., Kettyle, L.M., Luis, T.C., Norfo, R., Alcolea, V., Boukarabila, H., Grasso, F., Gambardella, A., Grover, A., et al. (2018). Hierarchically related lineage-restricted fates of multipotent haematopoietic stem cells. *Nature* 554, 106–111. <https://doi.org/10.1038/nature25455>.
48. Morcos, M.N.F., Li, C., Munz, C.M., Greco, A., Dressel, N., Reinhardt, S., Sameith, K., Dahl, A., Becker, N.B., Roers, A., et al. (2022). Fate mapping of hematopoietic stem cells reveals two pathways of native thrombopoiesis. *Nat. Commun.* 13, 4504. <https://doi.org/10.1038/s41467-022-31914-z>.
49. Carrelha, J., Mazzi, S., Winroth, A., Hagemann-Jensen, M., Ziegenhain, C., Högstrand, K., Seki, M., Brennan, M.S., Lehander, M., Wu, B., et al. (2024). Alternative platelet differentiation pathways initiated by nonhierarchically related hematopoietic stem cells. *Nat. Immunol.* 25, 1007–1019. <https://doi.org/10.1038/s41590-024-01845-6>.
50. Izzo, F., Lee, S.C., Poran, A., Chaligne, R., Gaiti, F., Gross, B., Murali, R.R., Deochand, S.D., Ang, C., Jones, P.W., et al. (2020). DNA methylation disruption reshapes the hematopoietic differentiation landscape. *Nat. Genet.* 52, 378–387. <https://doi.org/10.1038/s41588-020-0595-4>.
51. Nam, A.S., Dusaj, N., Izzo, F., Murali, R., Myers, R.M., Mouhieddine, T.H., Sotelo, J., Benbarche, S., Waarts, M., Gaiti, F., et al. (2022). Single-cell multi-omics of human clonal hematopoiesis reveals that DNMT3A R882 mutations perturb early progenitor states through selective hypomethylation. *Nat. Genet.* 54, 1514–1526. <https://doi.org/10.1038/s41588-022-01179-9>.
52. Uckelmann, H.J., Kim, S.M., Wong, E.M., Hatton, C., Giovinozzo, H., Gadrey, J.Y., Krivtsov, A.V., Rücker, F.G., Döhner, K., McGeehan, G.M., et al. (2020). Therapeutic targeting of preleukemia cells in a mouse model of NPM1 mutant acute myeloid leukemia. *Science* 367, 586–590. <https://doi.org/10.1126/science.aax5863>.
53. SanMiguel, J.M., Eudy, E., Loberg, M.A., Young, K.A., Mistry, J.J., Mujica, K.D., Schwartz, L.S., Stearns, T.M., Challen, G.A., and Trowbridge, J.J. (2022). Distinct tumor necrosis factor alpha Receptors Dictate Stem Cell Fitness versus Lineage Output in Dnmt3a-Mutant Clonal Hematopoiesis. *Cancer Discov.* 12, 2763–2773. <https://doi.org/10.1158/2159-8290.CD-22-0086>.
54. Brunetti, L., Gundry, M.C., Sorcini, D., Guzman, A.G., Huang, Y.-H., Ramabadran, R., Gionfriddo, I., Mezzasoma, F., Milano, F., Nabet, B., et al. (2018). Mutant NPM1 Maintains the Leukemic State through HOX

- Expression. *Cancer Cell* 34, 499–512.e9. <https://doi.org/10.1016/j.ccell.2018.08.005>.
55. Li, H., Mar, B.G., Zhang, H., Puram, R.V., Vazquez, F., Weir, B.A., Hahn, W.C., Ebert, B., and Pellman, D. (2017). The EMT regulator ZEB2 is a novel dependency of human and murine acute myeloid leukemia. *Blood* 129, 497–508. <https://doi.org/10.1182/blood-2016-05-714493>.
  56. Ono, R., Masuya, M., Nakajima, H., Enomoto, Y., Miyata, E., Nakamura, A., Ishii, S., Suzuki, K., Shibata-Minoshima, F., Katayama, N., et al. (2013). Plzf drives MLL-fusion-mediated leukemogenesis specifically in long-term hematopoietic stem cells. *Blood* 122, 1271–1283. <https://doi.org/10.1182/blood-2012-09-456665>.
  57. Mer, A.S., Heath, E.M., Madani Tonekaboni, S.A., Dogan-Artun, N., Nair, S.K., Murison, A., Garcia-Prat, L., Shlush, L., Hurren, R., Voisin, V., et al. (2021). Biological and therapeutic implications of a unique subtype of NPM1 mutated AML. *Nat. Commun.* 12, 1054. <https://doi.org/10.1038/s41467-021-21233-0>.
  58. Naldini, M.M., Casirati, G., Barcella, M., Rancoita, P.M.V., Cosentino, A., Caserta, C., Pavesi, F., Zonari, E., Desantis, G., Gillioli, D., et al. (2023). Longitudinal single-cell profiling of chemotherapy response in acute myeloid leukemia. *Nat. Commun.* 14, 1285. <https://doi.org/10.1038/s41467-023-36969-0>.
  59. Mann, R.S., and Affolter, M. (1998). Hox proteins meet more partners. *Curr. Opin. Genet. Dev.* 8, 423–429. [https://doi.org/10.1016/s0959-437x\(98\)80113-5](https://doi.org/10.1016/s0959-437x(98)80113-5).
  60. Li, Z., Zhang, Z., Li, Y., Arnovitz, S., Chen, P., Huang, H., Jiang, X., Hong, G.-M., Kunjamma, R.B., Ren, H., et al. (2013). PBX3 is an important cofactor of HOXA9 in leukemogenesis. *Blood* 121, 1422–1431. <https://doi.org/10.1182/blood-2012-07-442004>.
  61. Fennell, K.A., Vassiliadis, D., Lam, E.Y.N., Martelotto, L.G., Balic, J.J., Hollizeck, S., Weber, T.S., Semple, T., Wang, Q., Miles, D.C., et al. (2022). Non-genetic determinants of malignant clonal fitness at single-cell resolution. *Nature* 607, 125–131.
  62. Goyal, Y., Busch, G.T., Pillai, M., Li, J., Boe, R.H., Grody, E.I., Chelvanambi, M., Dardani, I.P., Emert, B., Bodkin, N., et al. (2023). Diverse clonal fates emerge upon drug treatment of homogeneous cancer cells. *Nature* 620, 651–659. <https://doi.org/10.1038/s41586-023-06342-8>.
  63. Schwartz, L.S., Young, K.A., Stearns, T.M., Boyer, N., Mujica, K.D., and Trowbridge, J.J. (2024). Transcriptional and functional consequences of Oncostatin M signaling on young Dnmt3a-mutant hematopoietic stem cells. *Exp. Hematol.* 130, 104131. <https://doi.org/10.1016/j.exphem.2023.11.005>.
  64. Uckelmann, H.J., Haarer, E.L., Takeda, R., Wong, E.M., Hatton, C., Marinaccio, C., Perner, F., Rajput, M., Antonissen, N.J.C., Wen, Y., et al. (2023). Mutant NPM1 Directly Regulates Oncogenic Transcription in Acute Myeloid Leukemia. *Cancer Discov.* 13, 746–765. <https://doi.org/10.1158/2159-8290.CD-22-0366>.
  65. Bowman, R.L., Dunbar, A.J., Mishra, T., Xiao, W., Waarts, M.R., Maestre, I.F., Eisman, S.E., Cai, L., Mowla, S., Shah, N., et al. (2024). In vivo models of subclonal oncogenesis and dependency in hematopoietic malignancy. *Cancer Cell* 42, 1955–1969.e7. <https://doi.org/10.1016/j.ccell.2024.10.009>.
  66. Tzelepis, K., Koike-Yusa, H., De Braekeleer, E., Li, Y., Metzakopian, E., Dovey, O.M., Mupo, A., Grinkevich, V., Li, M., Mazan, M., et al. (2016). A CRISPR Dropout Screen Identifies Genetic Vulnerabilities and Therapeutic Targets in Acute Myeloid Leukemia. *Cell Rep.* 17, 1193–1205. <https://doi.org/10.1016/j.celrep.2016.09.079>.
  67. Pei, S., Shelton, I.T., Gillen, A.E., Stevens, B.M., Gasparetto, M., Wang, Y., Liu, L., Liu, J., Brunetti, T.M., Engel, K., et al. (2023). A Novel Type of Monocytic Leukemia Stem Cell Revealed by the Clinical Use of Venetoclax-Based Therapy. *Cancer Discov.* 13, 2032–2049. <https://doi.org/10.1158/2159-8290.CD-22-1297>.
  68. Sango, J., Carcamo, S., Sirenko, M., Maiti, A., Mansour, H., Ulukaya, G., Tomalin, L.E., Cruz-Rodriguez, N., Wang, T., Olszewska, M., et al. (2024). RAS-mutant leukaemia stem cells drive clinical resistance to venetoclax. *Nature* 636, 241–250. <https://doi.org/10.1038/s41586-024-08137-x>.
  69. Levra Levrone, C., Watanabe, M., Proserpio, V., Piacenti, G., Lauria, A., Kaltenbach, S., Tamburrini, A., Nohara, T., Anselmi, F., Duval, C., et al. (2023). Tissue memory relies on stem cell priming in distal undamaged areas. *Nat. Cell Biol.* 25, 740–753. <https://doi.org/10.1038/s41556-023-01120-0>.
  70. Del Poggetto, E., Ho, I.-L., Balestrieri, C., Yen, E.-Y., Zhang, S., Citron, F., Shah, R., Corti, D., Diaferia, G.R., Li, C.-Y., et al. (2021). Epithelial memory of inflammation limits tissue damage while promoting pancreatic tumorigenesis. *Science* 373, eabj0486. <https://doi.org/10.1126/science.abj0486>.
  71. Alonso-Curbelo, D., Ho, Y.-J., Burdziak, C., Maag, J.L.V., Morris, J.P., 4th, Chandwani, R., Chen, H.-A., Tzanov, K.M., Barriga, F.M., Luan, W., et al. (2021). A gene-environment-induced epigenetic program initiates tumorigenesis. *Nature* 590, 642–648. <https://doi.org/10.1038/s41586-020-03147-x>.
  72. Chin, D.W.L., Yoshizato, T., Viriding Culleton, S., Grasso, F., Barbachowska, M., Ogawa, S., Jacobsen, S.E.W., and Woll, P.S. (2022). Aged healthy mice acquire clonal hematopoiesis mutations. *Blood* 139, 629–634. <https://doi.org/10.1182/blood.2021014235>.
  73. Kapadia, C.D., Williams, N., Dawson, K.J., Watson, C., Yousefzadeh, M.J., Le, D., Nyamondo, K., Cagan, A., Waldvogel, S., De La Fuente, J., et al. (2024). Clonal dynamics and somatic evolution of haematopoiesis in mouse. Preprint at bioRxiv. <https://doi.org/10.1101/2024.09.17.613129>.
  74. Ganuza, M., Hall, T., Finkelstein, D., Wang, Y.-D., Chabot, A., Kang, G., Bi, W., Wu, G., and McKinney-Freeman, S. (2019). The global clonal complexity of the murine blood system declines throughout life and after serial transplantation. *Blood* 133, 1927–1942. <https://doi.org/10.1182/blood-2018-09-873059>.
  75. Weinstock, J.S., Gopakumar, J., Burugula, B.B., Uddin, M.M., Jahn, N., Belk, J.A., Bouzid, H., Daniel, B., Miao, Z., Ly, N., et al. (2023). Aberrant activation of TCL1A promotes stem cell expansion in clonal haematopoiesis. *Nature* 616, 755–763. <https://doi.org/10.1038/s41586-023-05806-1>.
  76. Bick, A.G., Weinstock, J.S., Nandakumar, S.K., Fulco, C.P., Bao, E.L., Zekavat, S.M., Szeto, M.D., Liao, X., Leventhal, M.J., Nasser, J., et al. (2020). Inherited causes of clonal haematopoiesis in 97,691 whole genomes. *Nature* 586, 763–768. <https://doi.org/10.1038/s41586-020-2819-2>.
  77. Hormaechea-Agulla, D., Matatall, K.A., Le, D.T., Kain, B., Long, X., Kus, P., Jaksik, R., Challen, G.A., Kimmel, M., and King, K.Y. (2021). Chronic infection drives Dnmt3a-loss-of-function clonal hematopoiesis via IFN $\gamma$  signaling. *Cell Stem Cell* 28, 1428–1442.e6. <https://doi.org/10.1016/j.stem.2021.03.002>.
  78. Geurts, M.H., de Poel, E., Pleguezuelos-Manzano, C., Oka, R., Carrillo, L., Andersson-Rolf, A., Boretto, M., Brunsveld, J.E., van Boxtel, R., Beekman, J.M., et al. (2021). Evaluating CRISPR-based prime editing for cancer modeling and CFTR repair in organoids. *Life Sci. Alliance* 4, e20200940. <https://doi.org/10.26508/lsa.20200940>.
  79. Sommerkamp, P., Mercier, F.E., Wilkinson, A.C., Bonnet, D., and Bourguine, P.E. (2021). Engineering human hematopoietic environments through ossicle and bioreactor technologies exploitation. *Exp. Hematol.* 94, 20–25. <https://doi.org/10.1016/j.exphem.2020.11.008>.
  80. Frenz-Wiessner, S., Fairley, S.D., Buser, M., Goek, I., Salewskij, K., Jonsson, G., Illig, D., Zu Putlitz, B., Petersheim, D., Li, Y., et al. (2024). Generation of complex bone marrow organoids from human induced pluripotent stem cells. *Nat. Methods* 21, 868–881. <https://doi.org/10.1038/s41592-024-02172-2>.
  81. Khan, A.O., Rodriguez-Romera, A., Reyat, J.S., Olijnik, A.-A., Colombo, M., Wang, G., Wen, W.X., Sousos, N., Murphy, L.C., Grygielska, B., et al. (2023). Human Bone Marrow Organoids for Disease Modeling, Discovery, and Validation of Therapeutic Targets in Hematologic Malignancies. *Cancer Discov.* 13, 364–385. <https://doi.org/10.1158/2159-8290.CD-22-0199>.
  82. Chen, W., Guillaume-Gentil, O., Rainer, P.Y., Gäbelein, C.G., Saelens, W., Gardeux, V., Klaeger, A., Dainese, R., Zachara, M., Zambelli, T., et al.

- (2022). Live-seq enables temporal transcriptomic recording of single cells. *Nature* 608, 733–740. <https://doi.org/10.1038/s41586-022-05046-9>.
83. Benz, C., Martins, V.C., Radtke, F., and Bleul, C.C. (2008). The stream of precursors that colonizes the thymus proceeds selectively through the early T lineage precursor stage of T cell development. *J. Exp. Med.* 205, 1187–1199. <https://doi.org/10.1084/jem.20072168>.
84. Bindels, D.S., Haarbosch, L., van Weeren, L., Postma, M., Wiese, K.E., Mastop, M., Aumonier, S., Gotthard, G., Royant, A., Hink, M.A., et al. (2017). mScarlet: a bright monomeric red fluorescent protein for cellular imaging. *Nat. Methods* 14, 53–56. <https://doi.org/10.1038/nmeth.4074>.
85. Balleza, E., Kim, J.M., and Cluzel, P. (2018). Systematic characterization of maturation time of fluorescent proteins in living cells. *Nat. Methods* 15, 47–51. <https://doi.org/10.1038/nmeth.4509>.
86. Köster, J., and Rahmann, S. (2012). Snakemake—a scalable bioinformatics workflow engine. *Bioinformatics* 28, 2520–2522. <https://doi.org/10.1093/bioinformatics/bts480>.
87. Liu, D. (2019). Algorithms for efficiently collapsing reads with Unique Molecular Identifiers. *PeerJ* 7, e8275. <https://doi.org/10.7717/peerj.8275>.
88. Hao, Y., Stuart, T., Kowalski, M.H., Choudhary, S., Hoffman, P., Hartman, A., Srivastava, A., Molla, G., Madad, S., Fernandez-Granda, C., et al. (2024). Dictionary learning for integrative, multimodal and scalable single-cell analysis. *Nat. Biotechnol.* 42, 293–304. <https://doi.org/10.1038/s41587-023-01767-y>.
89. Germain, P.-L., Lun, A., Garcia Meixide, C., Macnair, W., and Robinson, M.D. (2021). Doublet identification in single-cell sequencing data using scDblFinder. *F1000Res* 10, 979. <https://doi.org/10.12688/f1000research.73600.2>.
90. Lun, A.T.L., Riesenfeld, S., Andrews, T., Dao, T.P., Gomes, T.; participants in the 1st Human Cell Atlas Jamboree, and Marioni, J.C. (2019). EmptyDrops: distinguishing cells from empty droplets in droplet-based single-cell RNA sequencing data. *Genome Biol.* 20, 63. <https://doi.org/10.1186/s13059-019-1662-y>.
91. Finak, G., McDavid, A., Yajima, M., Deng, J., Gersuk, V., Shalek, A.K., Slichter, C.K., Miller, H.W., McElrath, M.J., Pric, M., et al. (2015). MAST: a flexible statistical framework for assessing transcriptional changes and characterizing heterogeneity in single-cell RNA sequencing data. *Genome Biol.* 16, 278. <https://doi.org/10.1186/s13059-015-0844-5>.
92. Fang, Z., Liu, X., and Peltz, G. (2023). GSEAPy: a comprehensive package for performing gene set enrichment analysis in Python. *Bioinformatics* 39, btac757. <https://doi.org/10.1093/bioinformatics/btac757>.
93. Bibby, J.A., Agarwal, D., Freiwald, T., Kunz, N., Merle, N.S., West, E.E., Singh, P., Larochelle, A., Chinian, F., Mukherjee, S., et al. (2022). Systematic single-cell pathway analysis to characterize early T cell activation. *Cell Rep.* 41, 111697. <https://doi.org/10.1016/j.celrep.2022.111697>.
94. Alquicira-Hernandez, J., and Powell, J.E. (2021). Nebulosa recovers single-cell gene expression signals by kernel density estimation. *Bioinformatics* 37, 2485–2487. <https://doi.org/10.1093/bioinformatics/btab003>.
95. Blanco-Carmona, E. (2022). Generating publication ready visualizations for Single Cell transcriptomics using SCpubr. Preprint at bioRxiv. <https://doi.org/10.1101/2022.02.28.482303>.
96. Wilkinson, A.C., Ishida, R., Nakauchi, H., and Yamazaki, S. (2020). Long-term ex vivo expansion of mouse hematopoietic stem cells. *Nat. Protoc.* 15, 628–648. <https://doi.org/10.1038/s41596-019-0263-2>.
97. Bidy, B.A., Kong, W., Kamimoto, K., Guo, C., Waye, S.E., Sun, T., and Morris, S.A. (2018). Single-cell mapping of lineage and identity in direct reprogramming. *Nature* 564, 219–224. <https://doi.org/10.1038/s41586-018-0744-4>.

STAR★METHODS

KEY RESOURCES TABLE

REAGENT or RESOURCE	SOURCE	IDENTIFIER
<b>Antibodies</b>		
Anti-CD117 Microbeads mouse	Miltenyi Biotec	130-091-224
PE anti-mouse CD201	BioLegend	141504
APC anti-mouse c-Kit	BioLegend	135108
PE Cy7 anti-mouse Ly-6A/E (Sca-1)	BioLegend	108114
APC Cy7 anti-mouse CD48	BioLegend	103432
PE Cy5 anti-mouse CD150	BioLegend	115912
Pacific Blue Lineage Cocktail	BioLegend	133310
TotalSeq B0301 anti-mouse Hashtag1	BioLegend	155831
TotalSeq B0301 anti-mouse Hashtag2	BioLegend	155833
TotalSeq B0301 anti-mouse Hashtag3	BioLegend	155835
TotalSeq B0301 anti-mouse Hashtag4	BioLegend	155837
<b>Chemicals, peptides, and recombinant proteins</b>		
HEPES buffer solution	Gibco	15630-056
Insulin-Transferrin-Selenium-X	Gibco	51500-056
Poly (vinyl alcohol)	Sigma Aldrich	363081-1Kg
F-12 Nutrient Mix (Ham)	Gibco	21765-029
Direct PCR tail	Viagen	102-T
IBIAN-Proteinase K solution	IBIAN lab	106-PK01
LE Agarose	SeaKem	50004
LB Agar	PanReac AppliChem	A0927,1000KG
LB Medium	PanReac AppliChem	A0954,1000KG
NEB Builder Hifi DNA Assembly master Mix	New England Biolabs	M5520AA
KAPA2G Robust hotstar Ready Mix	KAPA Biosystems	KK5702
KAPA HiFi Hotstart Ready Mix	Roche	7958935001
Carbenicillin Disodium Salt	Thermo Scientific	10177-012
AMPure XP beads	Beckman Coulter	A63881
Fibronectin	R&D System	1030-FN-05M
Recombinant Murine TPO	Peptotech	315-14
Recombinant Murine SCF	Peptotech	250-03
Mouse IL-1 beta Recombinant Protein	Peptotech	211-11B
<b>Critical commercial assays</b>		
Chromium Next GEM Single Cell 3' Kit v3.1	10× Genomics	1000268
Chromium Next GEM Chip G Single Cell Kit	10× Genomics	1000127
Dual Index Kit TT Set A	10× Genomics	1000215
Dual Index Kit NT Set A	10× Genomics	1000250
NucleoBond Xtra Midi	Macherey-Nagel	740410.1
NucleoBond Xtra Maxi	Macherey-Nagel	740414.5
Nucleospin Plasmid	Macherey-Nagel	740588.25
Monarch Genomic DNA purification kit	New England Biolabs	10104305
<b>Deposited data</b>		
Analysis files and objects	This Paper	Zenodo: <a href="https://doi.org/10.5281/zenodo.14261507">https://doi.org/10.5281/zenodo.14261507</a>
Raw data for experiment 1-2 (ex vivo expansion)	This Paper	GEO: GSE266232

(Continued on next page)

**Continued**

REAGENT or RESOURCE	SOURCE	IDENTIFIER
Raw data for experiment 3 (in vivo, Flt3-Cre Npm1c)	This Paper	GEO: GSE282755
Raw data for experiment 4 (sequential mutagenesis)	This Paper	GEO: GSE282756
<b>Experimental models: Organisms/strains</b>		
C57BL/6- <i>Npm1tm1Trow/J</i>	The Jackson Laboratory	Strain #:033164; RRID:IMSR_JAX:033164
B6(Cg)- <i>Dnmt3atm1Trow/J</i>	The Jackson Laboratory	Strain #:032289; RRID:IMSR_JAX:032289
B6.Cg- <i>Gt(ROSA)26Sortm9(CAG-tdTomato)Hze/J</i>	The Jackson Laboratory	Strain #:007909; RRID:IMSR_JAX:007909
B6.129-Tg(Flt3-cre)#Ccb	Benz et al. <sup>83</sup>	RRID: EMMA EM:11790
<b>Recombinant DNA</b>		
pmScarlet_NES_C1	Bindels et al. <sup>84</sup>	Addgene plasmid # 85060; RRID:Addgene_85060
pEB1-T-Sapphire	Balleza et al. <sup>85</sup>	Addgene plasmid # 103977; RRID:Addgene_103977
pLARRY-EGFP	Weinreb et al. <sup>24</sup>	Addgene plasmid # 140025; RRID:Addgene_140025
pLARRYv2-T-Sapphire library 1	This Paper	Addgene plasmid #233213; RRID: Addgene_233213
pLARRYv2-T-Sapphire library 2	This Paper	Addgene plasmid #233214; RRID: Addgene_233214
pLARRYv2-T-Sapphire (backbone)	This Paper	Addgene plasmid #233209; RRID: Addgene_233209
pLARRYv2-EGFP library 1	This Paper	Addgene plasmid #233215; RRID: Addgene_233215
pLARRYv2-EGFP library 2	This Paper	Addgene plasmid #233216; RRID: Addgene_233216
pLARRYv2-EGFP (backbone)	This Paper	Addgene plasmid #233208; RRID: Addgene_233208
pLARRYv2-EGFP-T2A-Flpo (backbone)	This Paper	Addgene plasmid #233212; RRID: Addgene_233212
pLARRYv2-mScarlet-T2A-iCre (backbone)	This Paper	Addgene plasmid #233211; RRID: Addgene_233211
pLARRYv2-mScarlet (backbone)	This Paper	Addgene plasmid #233210; RRID: Addgene_233210
<b>Software and algorithms</b>		
FlowJo v10	BD	<a href="https://www.flowjo.com">https://www.flowjo.com</a>
GraphPad Prism 10	Dotmatics	<a href="http://www.graphpad.com">www.graphpad.com</a>
Affinity Designer	Serif	<a href="https://affinity.serif.com/en-us/">https://affinity.serif.com/en-us/</a>
Biorender	BioRender	<a href="https://app.biorender.com/">https://app.biorender.com/</a>
Snakemake	Köster et al. <sup>86</sup>	<a href="https://snakemake.github.io/">https://snakemake.github.io/</a>
UMICollapse	Liu et al. <sup>87</sup>	<a href="https://github.com/Daniel-Liu-c0deb0t/UMICollapse">https://github.com/Daniel-Liu-c0deb0t/UMICollapse</a>
CloneRanger v0.1.0	This Paper	<a href="https://github.com/dfernandezperez/cloneRanger">https://github.com/dfernandezperez/cloneRanger</a>
Seurat v5.0.1	Hao et al. <sup>88</sup>	<a href="https://satijalab.org/seurat/">https://satijalab.org/seurat/</a>
scDblFinder	Germain et al. <sup>89</sup>	<a href="https://doi.org/10.18129/B9.bioc.scDblFinder">https://doi.org/10.18129/B9.bioc.scDblFinder</a>
EmptyDrops	Lun et al. <sup>90</sup>	<a href="https://doi.org/10.18129/B9.bioc.DropletUtils">https://doi.org/10.18129/B9.bioc.DropletUtils</a>
MAST	Finak et al. <sup>91</sup>	<a href="https://rglab.github.io/MAST/">https://rglab.github.io/MAST/</a>
ComplexHeatmap v2.12.1	ComplexHeatmap	<a href="https://github.com/jokergoo/ComplexHeatmap">https://github.com/jokergoo/ComplexHeatmap</a>
Tidymverse v1.3.2	Tidymverse	<a href="https://www.tidymverse.org/">https://www.tidymverse.org/</a>
ggrastr v1.0.2	Ggrastr	<a href="https://github.com/VPetukhov/ggrastr">https://github.com/VPetukhov/ggrastr</a>
GSEAPy	Fang et al. <sup>92</sup>	<a href="https://github.com/zqfang/GSEAPy">https://github.com/zqfang/GSEAPy</a>
SCPA v1.6.2	Bibby et al. <sup>93</sup>	<a href="https://github.com/jackbibby1/SCPA/">https://github.com/jackbibby1/SCPA/</a>
SCpubr v2.0.2	Alquicira-Hernandez and Powell <sup>94</sup> Blanco-Carmona <sup>95</sup>	<a href="https://github.com/enblacar/SCpubr/">https://github.com/enblacar/SCpubr/</a>
cellranger v7.0.0	10x Genomics	<a href="https://www.10xgenomics.com/support/software/cell-ranger/latest">https://www.10xgenomics.com/support/software/cell-ranger/latest</a>

## EXPERIMENTAL MODEL AND STUDY PARTICIPANT DETAILS

### Animals

Rosa26-LSL-tdTomato, Dnmt3aLSL-R878H and Npm1frt-cA mice were obtained from The Jackson Laboratory, and alleles were maintained in a C57BL/6 background. B6 CD45.1 mice (B6.SJL-*Ptprc*<sup>a</sup> *Pepc*<sup>b</sup>/BoyJ) were purchased from Charles River France. Flt3-Cre mice were previously generated by Conrad Bleul<sup>83</sup> and kindly donated by Fernando Camargo (Boston Children's Hospital). All procedures involving animals adhered to the pertinent regulations and guidelines of the European Union, Spain, and Catalonia. Approval and oversight for all protocols and strains of mice were granted by the Institutional Review Board and the Institutional Animal Care and Use Committee at Parque Científico de Barcelona under protocol CEEA-PCB-22-001-ARF. The study follows all relevant ethical regulations. Mice were kept under specific pathogen-free conditions for all experiments. Eight to twelve-week-old male and female mice were tracked for the main experiments (donor 1 and 2, and donors 3 and 4), with exception of Flt3-Cre experiments for which only male mice were used (due to the Flt3 BAC Cre transgene being localized to the Y chromosome).

### Primary cell cultures

*Ex-vivo* cultures of HSCs were done under self-renewing F12-PVA-based conditions as described previously.<sup>32</sup> To this end, cell-culture activated 96-well flat-bottom plates were coated with a layer of 100 ng/ml fibronectin (Bovine Fibronectin Protein, CF Catalog: 1030-FN) for 30 minutes at room temperature. Following the sorting process, HSCs were transferred into 200  $\mu$ l of complete HSC media supplemented with 100 ng/ml recombinant mouse TPO and 10 ng/ml recombinant mouse SCF (PeproTech Recombinant Murine TPO Catalogue Number: 315-14; PeproTech Recombinant Murine SCF, Catalogue Number: 250-03) and grown at 37°C with 5% CO<sub>2</sub>. During lentiviral library transduction, the first media change took place 24 hours post-transduction. All other protocol steps followed the guidelines provided in Wilkinson et al.<sup>96</sup>

## METHOD DETAILS

### Hematopoietic stem cell isolation

Following euthanasia, bone marrow was harvested from the femur, tibia, pelvis, and sternum through mechanical crushing, ensuring the retrieval of most HSCs. The collected bone marrow cells were then sieved through a 100- $\mu$ m strainer and cleansed with a cold 'Easy Sep' buffer containing PBS with 2% fetal bovine serum (FBS), followed by lysis of red blood cells using RBC lysis buffer (Biolegend, Catalog no. 420302). At first, mature lineage cells were selectively depleted through the Lineage Cell Depletion Kit, mouse (Miltenyi Biotec, Catalog no. 130-110-470), while the resulting Lin<sup>-</sup> (lineage-negative) fraction was then enriched for c-Kit expression using CD117 MicroBeads (Miltenyi Biotec, Catalog no: 130-091-224). These cKit-enriched cells were washed, blocked with FcX and stained with following fluorescently labeled antibodies: APC anti-mouse CD117, clone ACK2 (Biolegend catalog no. 105812), PE/Cy7 anti-mouse Ly6a (Sca-1) (Biolegend, catalog no. 108114); Pacific Blue anti-mouse Lineage Cocktail (Biolegend, catalog no. 133310); PE anti-mouse CD201 (EPCR) (Biolegend, catalog no. 141504); PE/Cy5 anti-mouse CD150 (SLAM) (Biolegend, catalog no. 115912); APC/Cyanine7 anti-mouse CD48 (Biolegend, catalog no. 103432).

### Construction of lentiviral pLARRY vectors

The construction of barcoded libraries was executed by a previously established protocol (<https://www.protocols.io/view/barcode-plasmid-library-cloning-4hggt3w>). First, the T-Sapphire, Scarlett, or EGFP coding sequences, and the EF1a promoter sequences were PCR amplified from pEB1-T-Sapphire, pmScarlet\_NES\_C1, and pLARRY-EGFP with primers homologous to the vector insertion site in a custom synthetic lentiviral plasmid backbone (Vectorbuilder, Inc) using Gibson assembly (Gibson Assembly® Master Mix, NEB, Ref. E2611L). For recombinase lentivirus libraries, iCre or Flpo recombinase was PCR amplified together with EGFP and Scarlett with primers homologous to the vector insertion site in a custom synthetic lentiviral plasmid backbone and cloned using Gibson assembly. After magnetic-bead purification, ligated vectors were then transformed into NEB10-beta electroporation ultra-competent E.coli cells (NEB® 10-beta Electrocompetent E. coli, NEB, Ref.C3020K) and grown overnight on LB plates supplemented with 50  $\mu$ g/mL Carbenicillin (Carbenicillin disodium salt, Thermo Scientific Chemicals Ref. 11568616). Colonies were scrapped using LB medium and pelleted by centrifugation. Plasmid maxipreps were performed using the Endotoxin-Free Plasmid Maxi Kit (Machery Nagel), following the manufacturer's protocol. pEB1-T-Sapphire was a gift from Philippe Cluzel (Addgene plasmid 103977). pLARRY-EGFP was a gift from Fernando Camargo (Addgene plasmid 140025). pmScarlet\_NES\_C1 was a gift from Dorus Gadella (Addgene plasmid 85060).

### Barcode lentivirus library generation and diversity estimation

To barcode pLARRYv2 plasmids and generate a library, first a spacer sequence flanked by EcoRV restriction sites was cloned into the plasmid after the WPRE element of the vector. Custom PAGE-purified single-strand oligonucleotides with a pattern of 20 random bases and surrounded by 25 nucleotides homologous to the vector insertion site were synthesized by IDT DNA Technologies (Table S5). The assembly of these components and subsequent purification steps were carried out through Gibson assembly (Gibson Assembly® Master Mix, NEB, Ref. E2611L). Six electroporations of the bead-purified ligations were performed into NEB10-beta E.coli cells (NEB® 10-beta Electrocompetent E. coli, New England BiolabsEB, Ref.C3020K) utilizing a Gene Pulser electroporator (Biorad). Subsequently, after transformation, the cells were incubated at 37 degrees for 1 hour at 220 rpm. Post-incubation, the

transformed cells were plated in six large LB-ampicillin agar plates overnight at 30°C. Colonies from all six plates were collected by scraping with LB-ampicillin and then grown for an additional 2h at 225 rpm and 30 °C. Cultures were pelleted by centrifugation, and plasmids were isolated using the Endotoxin-Free Plasmid Maxi Kit (Machery-Nagel), following the manufacturer's protocol. For estimating diversity, barcode amplicon libraries were prepared by PCR amplification of the lentiviral library maxiprep using flanking oligonucleotides carrying TruSeq read1 and read2 adaptors using 10 ng of the library (Table S5). We used the minimal number of cycles that we could detect by qPCR to avoid PCR amplification bias (10-12 cycles). After bead purification, 10 ng of the first PCR product was used as a template for a second PCR to add Illumina P5 and P7 adaptors and indexes (Table S5). Two independent PCRs were sequenced on an Illumina NovaSeq 6000 S4 platform (Novogene UK) to confirm diversity after correction of errors through collapsing with a Hamming distance of 4. After collapsing, libraries were confirmed to contain at least 50 million different barcodes, with enough diversity for uniquely labeling up to 100,000 HSCs with a minimal false-positive rate (<1%). Sequencing results of these libraries are available at Zenodo (<https://doi.org/10.5281/zenodo.14261507>). Lentivirus production and HSPC transduction were performed as described in Weinreb et al.<sup>24</sup>

### Single-cell encapsulation and library preparation for sequencing

For scRNA sequencing and subsequent plating, cells were pipetted up and down gently a few times to be dissociated into single cells and transferred to a 1.5 mL microtube. The well was then washed with prewarmed PBS to collect all the possible remaining cells. Cells were then concentrated by centrifugation at 800 g for 8 minutes. Washed cells were then blocked with FcX, and stained with the E-SLAM stem cell antibodies panel, to confirm expansion of E-SLAM cells. Live cells were then sorted based on fluorescent reporter expression. Part of the sample as specified in text was then taken for constructing a single-cell library using Chromium Single Cell 3' Reagent Kits (v3) following the manufacturer's guidelines (10X Genomics). The remaining part was then plated back for further expansion in culture. To minimize the impact of batch effects on sequencing, we multiplexed different conditions leveraging the unique barcode pattern of our libraries together with Biolegend TotalSeq™ anti-mouse hashing antibodies (Table S5), enabling the simultaneous preparation of libraries representing all experimental conditions in a single reaction for each day of sampling.

Following the reverse transcription of mRNA and first-strand cDNA amplification, 100 ng of the cDNA libraries were used as templates to amplify LARRY barcodes by nested PCR similar to the protocol described in Weinreb et al.<sup>24</sup> The first PCR used forward primer (Pre-Enrichment forward) CTG AGC AAA GAC CCC AAC GAG AA together with the corresponding 10x Genomics dual index TruSeq reverse primer using the following programs 1, 98 C, 3 min; 2, 98 C, 20 s; 3, 58 C, 15 s; 4, 72 C, 20 s; 5, repeat steps 2–4 08 times; 6, 72 C, 3 min; 7, 4 C, hold. The PCR products were then purified with a 0.8:1 ratio of Ampure XP beads. Purified PCR products were then subjected to a second PCR using the forward primer (Truseq\_LARRY) GTG ACT GGA GTT CAG ACG TGT GCT CTT CCG ATC TGC TAG GAG AGA CCA TAT GGG ATC and the corresponding 10x dual index Truseq reserve primer, following program 1, 98 C, 3 min; 2, 98 C, 20 s; 3, 58 C, 15 s; 4, 72 C, 20 s; 5, repeat steps 2–4 08 times; 6, 72 C, 3 min; 7, 4 C, hold. The final PCR products were then purified by a 0.8:1 ratio of Ampure XP bead: PCR products, were indexed using the 10x dual index TruSeq kit, and sequenced using Illumina NovaSeq or NextSeq.

### scRNA-seq data processing and calling of lineage barcodes

Generation of single-cell matrices for gene expression and LARRY lineage barcodes was performed using *cloneRanger*, an in-house developed pipeline (<https://github.com/dfernandezperez/cloneRanger>) to process 10XGenomics single-cell RNA-seq together with LARRY barcoding. The pipeline is based on Snakemake<sup>86</sup> and the use of Docker/singularity containers to allow for reproducibility and easy deployment of the code.

For each sample, fastq files from gene expression (GEX), LARRY and TotalSeq™ tags were processed using *cellranger* v7.0.0 with default parameters. However, since *cellranger* only collapses barcodes that are 1 hamming distance apart, prior to the execution of *cellranger*, fastq files containing LARRY barcodes were processed using *UMICollapse*.<sup>87</sup> This allowed us to collapse all barcodes which were 4 hamming distance units apart or less, similar to the procedure used by Weinreb et al.<sup>24</sup> In particular, the *UMICollapse* was executed with the following parameters: “*fastq -k 4 -tag*”. Finally, in order to run *cellranger* in feature barcode mode with LARRY and TotalSeq™ sequences, we created a reference library csv file by extracting all detected LARRY barcodes across all collapsed fastq files, together with TotalSeq™ sequences. A reference library file was created for each individual sample and given as input to *cellranger*, executed with default parameters. All the code and steps performed by the pipeline are available in the *cloneRanger* github page.

A Seurat<sup>88</sup> object containing single-cell count matrices from GEX, LARRY and TotalSeq™ counts was created with the function *Read10X* from Seurat. Finally, cell doublets were removed with *scDblFinder*<sup>89</sup> using default parameters and TotalSeq™ sequences were demultiplexed with the function *hashedDrops* from the *DropletUtils* R package<sup>90</sup> with default parameters.

The assignment of LARRY barcodes to individual cells was performed by *cloneRanger* similarly to Weinreb et al.<sup>24</sup>: first, we generated a filtered LARRY matrix by removing barcode UMIs that were sustained by less than 5 sequencing reads (this information is stored in the *molecule\_info.h5* file generated by *cellranger*). Then, we further filtered the LARRY matrix by removing all barcodes with less than 4 UMIs. After filtering, barcodes were assigned to individual cells as following: (a) for cells in which only one barcode was detected after filtering, that barcode was assigned, (b) for cells in which more than one barcode was detected post-filtering, the top barcode with higher UMI counts was assigned and (c) for cells in which there were ties in the top barcode, no barcode was assigned. Our barcode calling strategy was developed to minimize mixing cells from different clones at the expenses of having higher chances to split real clones into subclones.

### Single-cell integration, clustering and annotation

To integrate scRNA-seq samples, we applied the *IntegrateLayers* Seurat v5 workflow to test multiple integration algorithms (sample time point was used as batch variable): Harmony, Reciprocal PCA, Canonical Correlation Analysis and Joint PCA. After supervising the results from all algorithms, we decided to use Reciprocal PCA to integrate the single-cell GEX matrices. We followed a standard Seurat pipeline with some minor modifications. Raw counts were normalized with the function *NormalizeData* and the top 3000 variable genes were selected. From those, we removed all ribosomal and mitochondrial genes, as well as genes that correlated with cell cycle genes (*Ube2c*, *Hmgb2*, *Hmgn2*, *Tuba1b*, *Ccnb1*, *Tubb5*, *Top2a*, *Tubb4b*, pearson cor of 0.1 or more), as performed by Weinreb et al.<sup>24</sup> Then, filtered variable genes were used to compute the top 50 reciprocal-PCA components. The kNN graph was computed using the function *FindNeighbors* setting the number of neighbors to 20, which was extended to 30 for the generation of UMAP components. Clusters were generated with the function *FindClusters* with a resolution of 0.3 and the Louvain algorithm.

Annotation of cell types was performed using known gene markers from the literature. A summary of the main markers for every cluster are shown in Figure S1B and the whole list of markers for every cluster, computed with *FindAllMarkers* from Seurat, are listed in Table S2. UMAPs and *Nebulosa* plots were performed using *SCpubr* v2.02.<sup>94,95</sup>

## QUANTIFICATION AND STATISTICAL ANALYSIS

### Quantification and classification of HSC clonal behaviors

Clone x state heatmaps from Figures 1, 2, and 4 were generated as follows: for every clone, we computed the number of cells detected across every cluster (cell type), generating a clone-by-cluster matrix A. In A, each  $A_{ij}$  represents the number of cells from the cluster  $j$  detected in the clone  $i$ . After generating A, in order to account for cell type abundance heterogeneity, we column-normalized the matrix by the total number of cells from each cell type, generating a B matrix. Finally, to compare clonal fates between clones of different sizes, we row-normalized the B matrix to obtain, for every clone, the fraction of cells present in each cell type (intra-clone fraction score).

HSC clonal behaviors were quantified as described in Rodriguez-Fraticelli et al.<sup>25,36</sup> based on the distribution of cells across HSC and non-HSC clusters. Output activity ( $A_i$ ) is quantified as the frequency of clone  $i$  non-HSC clusters divided by the frequency of clone  $i$  in the HSC cluster. Fate biases ( $B_i$ ) (megakaryocyte and myeloid) are calculated as the frequency of clone  $i$  in the cluster  $k$  divided by the frequency of the clone  $i$  across non- $k$  clusters (excluding also MPPs and HSC clusters).  $t$ . To determine statistically significant biased clones (clones representing a higher proportion of a specific cluster than expected from random cell sampling) we applied a Fisher's exact test as described in Bidy et al.<sup>97</sup> accounting for clone size.

### Sister cell similarity analysis

To calculate the sister cell similarity scores shown in Figure S1D, we subsetted individually the cells corresponding to each timepoint (Day 7 and D27) and proceeded as follows: The top 2000 variable genes were selected and, as described above, ribosomal, mitochondrial and genes correlating with cell cycle genes were filtered out. These filtered variable genes were scaled and used as input to calculate the top 70 principal components (PCs). The cell-by-PC matrix (obtained with the function *Embeddings* from Seurat) was used as input for the R *cor* function selecting *pearson* as the correlation metric. This procedure generated a cell-by-cell similarity matrix that was split into: (a) all pairs of sister cells, (b) all pairs of non-sister cells, and (c) all pairs of sister cells in which the barcode label was previously shuffled. To assess the statistical significance between the average Pearson coefficient of these 3 groups, a permutation test with 1000 simulations was performed. Briefly, the average correlation of each group was compared to a random distribution of sister similarity scores generated by shuffling the library barcodes prior to the generation of the cell-by-cell similarity matrix across 1000 iterations.

### Stochastic sampling model of clonal selection

To calculate the expected clonality across our experimental time course, assuming that all clones have equal fitness, we developed a null clonal selection model based on sampling with a binomial distribution. This model recapitulates the different sampling events (sample splitting, well splitting, sampling of cells for scRNA-seq, fraction of cells encapsulated in library preparation) and measured cell expansion (from D7 to D14 and D14 to D27). It makes two key assumptions for simplicity: no cell death (based on our limited observation of apoptotic-like events during culture) and similar proliferation probabilities for all cell types. We applied sequential sampling calls with and without replacement (using the R function *sample*) to model, from the initial distribution of clones sizes detected at D7, the following steps -using empirical data for each individual well replicate-: 1) fraction of cells lost in encapsulation for single-cell RNAseq at D7 (with replacement), 2) fraction of cells split into WT and mutant samples at D7 (without replacement), 3) transduction efficiency of secondary LARRY barcoding (without replacement), 4) fraction of cells split into different wells (without replacement), 5) cell expansion from D7 to D14 (with replacement), 6) fraction of cells used for D14 sequencing (without replacement), 7) cell expansion from D14 to D27 (with replacement), 8) fraction of cells sampled for D27 sequencing (without replacement) and 9) fraction of cell recovery (encapsulation) from D27 library preparation (without replacement). The output of the model is a list of the expected clones detected at D27 and their corresponding sizes. We ran 1000 iterations of the model, from which we calculated an average expected clone size. The distribution of clones sizes from the model was also used to calculate the expected clone size correlation between wells at D27.

### Single-cell differential gene expression and signature scores

Gene differential expression analysis corresponding to [Figures 3, 5, and 6](#) were performed using a Wilcoxon test with the function *findMarkers* from Seurat. Gene differential expression analysis corresponding to the data presented in [Figures 1, 2, and 4](#) were performed using MAST<sup>91</sup> within the function *findMarkers* from Seurat using the replicate information as the only latent variable. This was done in order to mask differences in gene expression between male and female cells, which corresponded to replicate 1 and replicate 2, respectively.

### Gene set enrichment analysis

For each comparison, we created pre-ranked lists based on  $\log_2$  fold-change differences in gene expression obtained from scRNA-seq or bulkRNAseq analysis. These pre-ranked lists were analyzed using *gseapy* version 1.1.1.<sup>92</sup> For gene sets, we used signatures shown on [Table S4](#) (HSC signatures) or MsigDB gene sets (mouse hallmarks or gene-ontology terms). Data from AML patients were obtained from previous studies.<sup>57,58</sup> For the scRNAseq dataset, patients were categorized as “mature” or “primitive” based on the ratio of % cells expressing CD14 versus % cells expressing CD96. Patients with CD14/CD96 ratio  $>1$  were labeled as “mature”, while CD14/CD96 ratio  $<1$  were labeled as “primitive”. For the bulkRNAseq dataset, we used the differential expression list output in the available code (comparing the “mature” patient cluster with the “primitive” patient cluster).

For [Figure 6](#) panel E, SCPA v1.6.2 was used to perform gene set enrichment analysis, using the same gene sets described in the previous paragraph<sup>93</sup> Gene sets with a  $-\log_{10}(\text{qvalue}) > 2$  and adjusted p-value  $< 0.01$  were considered as significantly enriched.

### Additional data visualization and figure preparation

For additional arranging and visualization of clonal data we used Tidyverse v1.3.2, ggrastr and ComplexHeatmap (see [key resources table](#)).

### Statistical methods

Statistical analysis was performed using the tests as indicated throughout the main text and in the Figure Legends. Wilcoxon rank-sum tests (adjusted for multiple comparisons where necessary) were used for statistical significance except where indicated. Statistical significance was generally defined as  $p < 0.05$ , unless otherwise specified. No exclusion or inclusion criteria were used. No strategies for blinding or randomization were used. For statistical analysis, we used Wilcoxon tests, which avoid specific assumptions about data distributions.